

Phenomenological anatomy of top-quark FCNCs induced by a light scalar singlet

Biao-Feng Hou,^a Xin-Qiang Li,^{a,b} Ya-Dong Yang,^{a,c} Xing-Bo Yuan^a and Ming-Wang Zhang^a

^a*Institute of Particle Physics and Key Laboratory of Quark and Lepton Physics (MOE), Central China Normal University, Wuhan, Hubei 430079, China*

^b*Center for High Energy Physics, Peking University, Beijing 100871, China*

^c*Institute of Particle and Nuclear Physics, Henan Normal University, Xinxiang 453007, China*

E-mail: resonhou@zknu.edu.cn, xqli@mail.ccnu.edu.cn, yangyd@ccnu.edu.cn, y@ccnu.edu.cn, mwzhang@mails.ccnu.edu.cn

ABSTRACT: Scalar singlets under the Standard Model gauge group appear naturally in many well-motivated New Physics scenarios, such as the composite Higgs models. Unlike the Higgs boson in the Standard Model, they can induce large flavour-changing neutral currents (FCNCs) in the top sector. We investigate systematically the effects of a light scalar singlet S with top-quark FCNC couplings, by including the low-energy constraints from the $B_s \rightarrow \mu^+ \mu^-$ decay, the muon anomalous magnetic moment $(g-2)_\mu$ and the neutron Electric Dipole Moment (EDM). We also perform a detailed Monte-Carlo simulation of the channel $pp \rightarrow tS + j$ with $S \rightarrow \mu^+ \mu^-$ and $S \rightarrow b\bar{b}$, and investigate the LHC sensitivity to the tcS couplings. It is found that the scalar singlet S can induce scalar-type contributions to the $B_s \rightarrow \mu^+ \mu^-$ decay, which do not suffer from the helicity suppression and contain a large CKM factor $V_{cs}^* V_{tb}$. As a result, constraints on the tcS couplings from the measured branching ratio $\mathcal{B}(B_s \rightarrow \mu^+ \mu^-)$ are quite stringent, being even stronger than the expected LHC sensitivity in some parameter spaces. Besides the CP-conserving tcS couplings, we have also considered the case of CP-violating tcS couplings, with $y_{R,L}^{ct} = |y_{R,L}^{ct}| e^{i\theta_{R,L}}$. It is found that the CP observables $\mathcal{A}_{\Delta\Gamma_s}^{\mu\mu}$ and $\mathcal{S}_{\mu\mu}$ of the $B_s \rightarrow \mu^+ \mu^-$ decay are sensitive to the phase θ_R , while the neutron EDM can provide bounds on the phase difference $\theta_L - \theta_R$. Therefore, they are complementary to each other in probing the CP phases of the tcS couplings.

Contents

1	Introduction	1
2	Effective Lagrangian	4
3	Low-energy constraints	5
3.1	$B_s \rightarrow \mu^+ \mu^-$ decay	5
3.2	Muon $g - 2$	10
3.3	Neutron EDM	11
4	Phenomenology at the LHC	14
4.1	Three-lepton final states through $S \rightarrow \mu^+ \mu^-$ channel	16
4.2	Three- b -jet final states through $S \rightarrow b\bar{b}$ channel	19
4.3	Multiple final states	21
5	Combined analysis	22
5.1	CP-conserving tcS couplings	22
5.2	CP-violating tcS couplings	24
6	Conclusions	31
A	Combined analysis in the scalar and pseudoscalar basis	32

1 Introduction

One major focus of the Large Hadron Collider (LHC) and its high-luminosity upgrade is the direct searches for new particles beyond the Standard Model (SM) [1]. While no credible signals have been found at the LHC so far, these searches are placing significant constraints on many New Physics (NP) models [2]. For many NP resonances, the current exclusion limits at the LHC have reached up to TeV or even multi-TeV scale [3], e.g., lower limits for some particular types of Z' particles range from around 4 to 5 TeV [4, 5]. However, most of these limits rely on the couplings of the resonances to the first two generations, or assume flavour universal interactions. Alternatively, searches for new particles in top-quark related processes are also well motivated, since its large mass makes the top quark connect inherently to the origin of electroweak (EW) symmetry breaking [6–8].

At the LHC, top quarks are copiously produced and searches for new particles in its rare decays hold, therefore, great promise. In this respect, the top-quark

flavour-changing neutral current (FCNC) decays involving a new light scalar singlet (S) are regarded as an excellent probe of NP effects [9, 10]. The light scalar singlets are naturally present in many NP scenarios, including the Next-to-Minimal Supersymmetric Standard Model [11], the Composite Higgs Models (CHM) [12–15], the Froggatt-Nielsen mechanism of flavour structures [16], and the EW Baryogenesis [17, 18]. The top-quark FCNC couplings mediated by the scalar singlet S may not be suppressed by the Glashow-Iliopoulos-Maiani mechanism, and thus significantly larger than those induced by the SM Higgs boson [19, 20], as noticed in the CHM [21, 22]. From the viewpoint of Effective Field Theory (EFT), the S -mediated FCNCs arise from dim-5 operators and thus less suppressed by one power of v/Λ compared to those induced by the SM Higgs boson, which arise firstly at dim 6. Moreover, unlike the SM Higgs boson, the scalar singlet S can decay into clean final states with relatively large branching ratios, such as $S \rightarrow \mu^+\mu^-$ and $S \rightarrow b\bar{b}$. In light of these considerations, search strategies for such scalar singlets have been investigated at the LHC through the channels $pp \rightarrow tS + j$, with $S \rightarrow \mu^+\mu^-$ or $S \rightarrow b\bar{b}$ [21, 22]. Recently, the ATLAS collaboration has also performed a search for the scalar singlet in top-quark FCNC decays $t \rightarrow qS$, with $q = u, c$ and $S \rightarrow b\bar{b}$ [23]. The obtained upper bounds on the branching ratio $\mathcal{B}(t \rightarrow cS)$ are between 1.8×10^{-4} and 7.8×10^{-4} for the scalar masses between 20 and 160 GeV.

The top-quark FCNCs mediated by new particles could also affect low-energy processes via the top-quark loops, such as the B -meson FCNC decays. In this respect, the $B_s \rightarrow \mu^+\mu^-$ decay is one of the most promising processes, which has already played an important role in constraining physics beyond the SM [24–28]. Recently, significant progress has been made in measuring this rare decay by the ATLAS [29], CMS [30], and LHCb [31, 32] collaborations at the LHC. Their measured time-integrated branching fractions read

$$\begin{aligned}\mathcal{B}(B_s \rightarrow \mu^+\mu^-)_{\text{ATLAS}} &= (2.8_{-0.7}^{+0.8}) \times 10^{-9}, \\ \mathcal{B}(B_s \rightarrow \mu^+\mu^-)_{\text{CMS}} &= (3.83_{-0.36-0.16-0.13}^{+0.38+0.19+0.14}) \times 10^{-9}, \\ \mathcal{B}(B_s \rightarrow \mu^+\mu^-)_{\text{LHCb}} &= (3.09_{-0.43-0.11}^{+0.46+0.15}) \times 10^{-9}.\end{aligned}\tag{1.1}$$

Based on these results, the current Particle Data Group world average is given by [2]

$$\mathcal{B}(B_s \rightarrow \mu^+\mu^-)_{\text{exp}} = (3.34 \pm 0.27) \times 10^{-9}.\tag{1.2}$$

Within the SM, by including the QCD corrections up to next-to-next-to-leading order (NNLO) [33–36] and the next-to-leading order (NLO) EW correction [37], the branching ratio is predicted to be

$$\mathcal{B}(B_s \rightarrow \mu^+\mu^-)_{\text{SM}} = (3.51 \pm 0.09) \times 10^{-9},\tag{1.3}$$

which is based on the calculations performed in refs. [38, 39] but with updated input parameters. For recent studies on the QED corrections, we refer to refs. [40–42]. The

above SM prediction is in good agreement with the current experimental average. Relevant studies in NP scenarios can be found, e.g., in refs. [43–49].

In this work, we will perform a systematic investigation of the top-quark FCNCs mediated by a new scalar singlet in the EFT framework, especially by including several low-energy constraints. Considering searches for such a singlet through the channel $pp \rightarrow tS + j$ with $S \rightarrow \mu^+\mu^-$, the involved tcS and $\mu\mu S$ couplings can also enter the $B_s \rightarrow \mu^+\mu^-$ decay at the one-loop level. It will be shown that this contribution results in the effective operators $(\bar{s}P_R b)(\bar{\mu}\mu)$ and $(\bar{s}P_R b)(\bar{\mu}\gamma_5\mu)$ at the scale of m_b , with m_b being the bottom-quark mass. Unlike the dominant SM contribution from $(\bar{s}\gamma^\mu P_L b)(\bar{\mu}\gamma_\mu\gamma_5\mu)$, these NP effects do not suffer from the helicity suppression. Furthermore, they are proportional to the CKM factor $V_{cs}^*V_{tb}$, which is much larger than $V_{ts}^*V_{tb}$ of the SM contribution. Therefore, it is crucial to study constraints on the scalar singlet S from the $B_s \rightarrow \mu^+\mu^-$ decay. In order to constrain the $\mu\mu S$ coupling, bounds from the muon anomalous magnetic moment $(g-2)_\mu$ will also be considered. In addition, we will perform a detailed collider simulation, considering both the rare top decay $t \rightarrow qS$ and the single top production associated with an S at the LHC, with the decay channels $S \rightarrow b\bar{b}$ and $S \rightarrow \mu^+\mu^-$.

It is also noted that the tqS couplings can be complex in general [25], which is however difficult to access at the LHC by analyzing only the cleanest decay final states like $\mu^+\mu^-$ and $b\bar{b}$. On the other side, besides the branching ratio, the $B_s \rightarrow \mu^+\mu^-$ decay offers other CP related observables, $\mathcal{A}_{\Delta\Gamma_s}^{\mu\mu}$ and $\mathcal{S}_{\mu\mu}$, due to the sizable decay width difference of the B_s system [44, 50]. These CP observables are theoretically clean and can provide information on the CP-violating contributions from NP [27, 51]. Therefore, it is interesting to explore the potential of these CP observables in revealing the CP-violating tqS interactions. In addition, the neutron Electric Dipole Moment (EDM) can generally provide extremely sensitive probes of new sources of CP violation beyond the SM [52–55]. We will, therefore, investigate the neutron EDM constraint on the tqS couplings and explore its complementarity with the $B_s \rightarrow \mu^+\mu^-$ decay.

The article is organized as follows. In section 2, we introduce the EFT Lagrangian to describe the interactions between the scalar singlet S and the SM fermions with top-quark FCNC couplings. In section 3, we recapitulate the theoretical frameworks for the $B_s \rightarrow \mu^+\mu^-$ decay, $(g-2)_\mu$ and the neutron EDM, and investigate constraints from these low-energy processes. In section 4, we perform a detailed collider simulation and explore the phenomenology of $pp \rightarrow tS + j$ with $S \rightarrow \mu^+\mu^-$ and $S \rightarrow b\bar{b}$ at the LHC. In section 5, we investigate the scalar singlet effects on the processes discussed in the last two sections, with both CP-conserving and CP-violating tcS couplings. Our conclusions are finally made in section 6. In appendix A, a combined analysis of the CP-violating tcS couplings is performed in the scalar and pseudoscalar basis (i.e., in terms of the couplings y_S^{ct} and y_P^{ct}), instead of the chiral basis (i.e., in terms of the couplings y_L^{ct} and y_R^{ct}) as discussed in subsection 5.2.

2 Effective Lagrangian

In order to describe the interactions between the scalar singlet S and the SM fermions, we adopt the EFT approach proposed in refs. [21, 22, 56]. After the EW symmetry breaking, the most general effective Lagrangian governing the tqS interaction reads

$$\mathcal{L}_S \supset -\frac{1}{\sqrt{2}}S[\bar{q}(y_S^{qt} + iy_P^{qt}\gamma^5)t + \text{h.c.}], \quad (2.1)$$

where $q = u, c$, and the scalar and fermions are all given in the mass eigenbasis. Such interactions arise from the gauge invariant dim-5 operator $(\bar{q}_L \tilde{H} Y u_R)S$, where q_L denotes the SM left-handed quark doublet, u_R the SM right-handed quark singlet, $\tilde{H} = i\sigma_2 H$ with H being the SM Higgs doublet, and Y the 3×3 complex matrix in flavour space. Considering the direct searches for the scalar singlet S through the top-quark FCNC decay $t \rightarrow cS$ with $S \rightarrow \mu^+\mu^-(b\bar{b})$ at the LHC, we also include the following flavour-conserving interactions [21, 22, 56]:

$$\mathcal{L}_S \supset -\frac{1}{\sqrt{2}}S[\bar{\mu}(y_S^{\mu\mu} + iy_P^{\mu\mu}\gamma^5)\mu + \bar{b}(y_S^{bb} + iy_P^{bb}\gamma^5)b]. \quad (2.2)$$

It is noted that the flavour-conserving couplings $y_{S,P}^{\mu\mu}$ and $y_{S,P}^{bb}$ are both real by definition, whereas the top-quark FCNC couplings $y_{S,P}^{qt}$ can be complex in general. Besides the scalar and pseudoscalar basis as defined above, it is also convenient to describe the couplings of the scalar singlet S with the SM fermions in the chiral basis of y_L^{ij} and y_R^{ij} , with $y_{R,L}^{ij} \equiv y_S^{ij} \pm iy_P^{ij}$.

The effective Lagrangian in eqs. (2.1) and (2.2) has been widely adopted in the investigation of direct searches for the top-quark FCNC processes induced by the scalar singlet S at the LHC [9, 21, 22]. Its UV completion has been studied in refs. [21, 57]. Generally, the scalar S can have other couplings in addition to those introduced in eqs. (2.1) and (2.2). For example, considering the $S\tau^+\tau^-$ and $S\gamma\gamma$ couplings, the LHC searches for the top-quark FCNCs with the scalar S through the $S \rightarrow \tau^+\tau^-$ and $S \rightarrow \gamma\gamma$ channels have been studied in refs. [22] and [21], respectively. In addition, the flavour-conserving couplings of S to the quarks can be assessed through the direct searches for the scalar resonances as performed, e.g., in ref. [58]. In this work, we concentrate on the couplings introduced in eqs. (2.1) and (2.2). This is motivated by the observation that our main conclusions would not be altered by including other couplings, since they cannot affect the collider processes and the low-energy constraints we are considering here simultaneously. For detailed studies of the flavour structure of the scalar singlet S , we refer to refs. [16, 59, 60].

With the effective interactions specified by eq. (2.2), the scalar S can only decay into $b\bar{b}$ and/or $\mu^+\mu^-$. Their decay widths can be written as

$$\Gamma(S \rightarrow f\bar{f}) = N_C \frac{m_S}{16\pi} \left[(y_S^{ff})^2 \beta_f^3 + (y_P^{ff})^2 \beta_f \right], \quad (2.3)$$

with $\beta_f = \sqrt{1 - 4x_f}$ and $x_f = m_f^2/m_S^2$ for $f = b$ or μ . The colour factor $N_C = 1$ for $f = \mu$, and $N_C = 3$ for $f = b$. In the case of $m_t > m_S + m_c$, the top quark can even decay into an on-shell S and a charm quark, with the decay width given by

$$\Gamma(t \rightarrow cS) = \frac{3m_t}{32\pi} \left(|y_S^{ct}|^2 + |y_P^{ct}|^2 \right) \left(1 - \frac{m_S^2}{m_t^2} \right)^2. \quad (2.4)$$

Then, the branching ratio can be written as $\mathcal{B}(t \rightarrow cS) \approx \Gamma(t \rightarrow cS)/\Gamma(t \rightarrow bW)$. For the $t \rightarrow bW$ decay, the recent NNLO calculation gives $\Gamma(t \rightarrow bW) = 1.33 \text{ GeV}$ [61]. When the scalar mass is much higher than the EW scale, the top quark cannot decay into an on-shell S . In this case, the effects of the scalar S are adequately described by the four-fermion operators investigated in refs. [62, 63].

3 Low-energy constraints

In this section, we investigate the relevant low-energy processes affected by the scalar singlet S , including the $B_s \rightarrow \mu^+\mu^-$ decay, $(g-2)_\mu$ and the neutron EDM.

3.1 $B_s \rightarrow \mu^+\mu^-$ decay

The rare decay $B_s \rightarrow \mu^+\mu^-$ is induced by the quark-level $b \rightarrow s\mu^+\mu^-$ transition in the SM, as shown by the first three Feynman diagrams in figure 1. Due to the helicity, loop and CKM suppression, the decay provides very promising probes of NP effects. With the scalar S contribution taken into account, the low-energy effective Hamiltonian governing the $B_s \rightarrow \mu^+\mu^-$ decay reads [51, 64]

$$\mathcal{H}_{\text{eff}} \supset -\frac{G_F\alpha_e}{\sqrt{2}\pi} V_{ts}^* V_{tb} [\mathcal{C}_{10}\mathcal{O}_{10} + \mathcal{C}_S\mathcal{O}_S + \mathcal{C}_P\mathcal{O}_P] + \text{h.c.}, \quad (3.1)$$

where V_{ij} denote the CKM matrix elements. The semi-leptonic four-fermion operators \mathcal{O}_i are defined, respectively, by

$$\mathcal{O}_{10} = (\bar{s}\gamma^\mu P_L b)(\bar{\mu}\gamma_\mu\gamma_5\mu), \quad \mathcal{O}_S = m_b(\bar{s}P_R b)(\bar{\mu}\mu), \quad \mathcal{O}_P = m_b(\bar{s}P_R b)(\bar{\mu}\gamma_5\mu), \quad (3.2)$$

with the chiral projectors given by $P_{L,R} = (1 \mp \gamma_5)/2$. In the SM, the Wilson coefficient \mathcal{C}_{10} arises firstly at the one-loop level, with the contributing Feynman diagrams shown by the first three in figure 1. Corrections up to the NNLO QCD [33–36] and the NLO EW [37] have been calculated, which result in $\mathcal{C}_{10}^{\text{SM}} = -4.17$ at the scale $\mu = 4.8 \text{ GeV}$ [38]. In addition, the Wilson coefficients \mathcal{C}_S and \mathcal{C}_P in the SM are induced by the Higgs-penguin diagrams and are highly suppressed [45, 65, 66]. Therefore, they can be safely neglected, i.e., $\mathcal{C}_S^{\text{SM}} \approx \mathcal{C}_P^{\text{SM}} \approx 0$.

In terms of the effective Lagrangian introduced in section 2, the tcS interaction can also affect the $b \rightarrow s\mu^+\mu^-$ transition through the scalar-penguin diagram shown in figure 1 (d). We evaluate this contribution in the unitary gauge with the modified

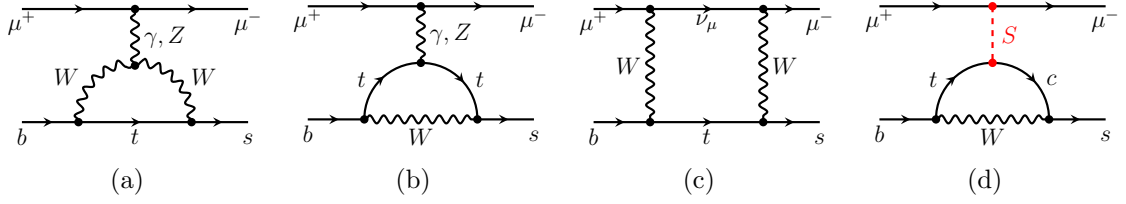


Figure 1: One-loop Feynman diagrams for the $b \rightarrow s\mu^+\mu^-$ transition, including both the dominant SM (the first three) and the scalar S contribution (the last one).

minimal subtraction ($\overline{\text{MS}}$) scheme. It is found that only the Wilson coefficients \mathcal{C}_S and \mathcal{C}_P are affected and take the form

$$\begin{aligned}\mathcal{C}_S^{\text{NP}}(\mu_W) &= \frac{y_S^{\mu\mu} y_R^{ct} V_{cs}^* m_t}{8\pi\alpha_e V_{ts}^* m_S^2} \cdot F(x_t), \\ \mathcal{C}_P^{\text{NP}}(\mu_W) &= \frac{iy_P^{\mu\mu} y_R^{ct} V_{cs}^* m_t}{8\pi\alpha_e V_{ts}^* m_S^2} \cdot F(x_t),\end{aligned}\tag{3.3}$$

with $y_R^{ct} = y_S^{ct} + iy_P^{ct}$, $x_t \equiv m_t^2/m_W^2$ and the loop function given by

$$F(x) = \frac{1}{2} \ln \frac{\mu_W^2}{m_W^2} + \frac{7-x}{4(1-x)} + \frac{2+2x-x^2}{2(1-x)^2} \ln x.\tag{3.4}$$

It is noted that, compared to $\mathcal{C}_{10}^{\text{SM}}$, both $\mathcal{C}_S^{\text{NP}}$ and $\mathcal{C}_P^{\text{NP}}$ could be largely enhanced by the CKM factor V_{cs}^*/V_{ts}^* .

With the effective Hamiltonian in eq. (3.1), the theoretical branching ratio of the $B_s \rightarrow \mu^+\mu^-$ decay can be expressed as [44, 50]

$$\mathcal{B}(B_s \rightarrow \mu^+\mu^-) = \frac{G_F^2 \alpha_e^2}{64\pi^3} m_{B_s} \tau_{B_s} f_{B_s}^2 |V_{tb} V_{ts}^*|^2 4m_\mu^2 \sqrt{1 - \frac{4m_\mu^2}{m_{B_s}^2}} |\mathcal{C}_{10}^{\text{SM}}|^2 (|P|^2 + |S|^2),\tag{3.5}$$

where m_{B_s} , $\tau_{B_s} = 1/\Gamma_s$ and f_{B_s} denote the mass, lifetime and decay constant of the B_s meson, respectively. The quantities P and S are defined as

$$\begin{aligned}P &= 1 + \frac{m_{B_s}^2}{2m_\mu} \left(\frac{m_b}{m_b + m_s} \right) \frac{\mathcal{C}_P}{\mathcal{C}_{10}^{\text{SM}}} \equiv |P|e^{i\varphi_P}, \\ S &= \sqrt{1 - \frac{4m_\mu^2}{m_{B_s}^2}} \frac{m_{B_s}^2}{2m_\mu} \left(\frac{m_b}{m_b + m_s} \right) \frac{\mathcal{C}_S}{\mathcal{C}_{10}^{\text{SM}}} \equiv |S|e^{i\varphi_S},\end{aligned}\tag{3.6}$$

where φ_P and φ_S denote the CP-violating phases of P and S , respectively.

Taking into account the sizable width difference of the B_s system, the experimentally measured branching ratio of the $B_s \rightarrow \mu^+\mu^-$ decay should be the time-integrated one [44, 50], which is related to eq. (3.5) through

$$\overline{\mathcal{B}}(B_s \rightarrow \mu^+\mu^-) = \left(\frac{1 + \mathcal{A}_{\Delta\Gamma_s}^{\mu\mu} y_s}{1 - y_s^2} \right) \mathcal{B}(B_s \rightarrow \mu^+\mu^-),\tag{3.7}$$

with

$$y_s = \frac{\Gamma_s^L - \Gamma_s^H}{\Gamma_s^L + \Gamma_s^H} = \frac{\Delta\Gamma_s}{2\Gamma_s}. \quad (3.8)$$

Here $\Delta\Gamma_s = \Gamma_s^L - \Gamma_s^H$ is the width difference of the B_s system, and Γ_s^L and Γ_s^H denote the decay widths of the light and heavy B_s mass eigenstates, respectively. Note that throughout this paper, unless otherwise specified, we use $\mathcal{B}(B_s \rightarrow \mu^+\mu^-)$ to denote the time-integrated branching ratio defined by eq. (3.7), and confront it with the experimental data given in eq. (1.2). With the effective interactions in eq. (2.1), the scalar singlet S does not affect the B_s - \bar{B}_s mixing. In this case, the mass-eigenstate rate asymmetry $\mathcal{A}_{\Delta\Gamma_s}^{\mu\mu}$ can be written as

$$\mathcal{A}_{\Delta\Gamma_s}^{\mu\mu} = \frac{|P|^2 \cos 2\varphi_P - |S|^2 \cos 2\varphi_S}{|P|^2 + |S|^2}, \quad (3.9)$$

which is equal to +1 in the SM but can vary between -1 and +1 in the presence of NP contributions. $\mathcal{A}_{\Delta\Gamma_s}^{\mu\mu}$ can be obtained via the following relation [27, 50]:

$$\mathcal{A}_{\Delta\Gamma_s}^{\mu\mu} = \frac{1}{y_s} \left[\frac{(1 - y_s^2)\tau_{\mu\mu}^s - (1 + y_s^2)\tau_{B_s}}{2\tau_{B_s} - (1 - y_s^2)\tau_{\mu\mu}^s} \right], \quad (3.10)$$

by measuring the effective lifetime $\tau_{\mu\mu}^s$ of the $B_s \rightarrow \mu^+\mu^-$ decay. The current experimental measurements of $\tau_{\mu\mu}^s$ can then be translated into bounds on $\mathcal{A}_{\Delta\Gamma_s}^{\mu\mu}$, yielding

$$\mathcal{A}_{\Delta\Gamma_s}^{\mu\mu} = \begin{cases} 8.44 \pm 7.11 & \text{LHCb [31],} \\ 3.75 \pm 3.68 & \text{CMS [30],} \\ -4.08 \pm 2.52 & \text{ATLAS [67],} \end{cases} \quad (3.11)$$

the uncertainties of which are still too large compared to the model-independent range of $-1 \leq \mathcal{A}_{\Delta\Gamma_s}^{\mu\mu} \leq +1$.

We can also consider the fully time-dependent and flavour-tagged rate of the $B_s \rightarrow \mu^+\mu^-$ decay with specific helicity configurations of the two muon final states. Then, the helicity-dependent rate asymmetry can be defined as [44, 50]

$$\frac{\Gamma(B_s^0(t) \rightarrow \mu_\lambda^+ \mu_\lambda^-) - \Gamma(\bar{B}_s^0(t) \rightarrow \mu_\lambda^+ \mu_\lambda^-)}{\Gamma(B_s^0(t) \rightarrow \mu_\lambda^+ \mu_\lambda^-) + \Gamma(\bar{B}_s^0(t) \rightarrow \mu_\lambda^+ \mu_\lambda^-)} = \frac{\mathcal{C}_{\mu\mu}^\lambda \cos(\Delta M_s t) + \mathcal{S}_{\mu\mu} \sin(\Delta M_s t)}{\cosh(y_s t / \tau_{B_s}) + \mathcal{A}_{\Delta\Gamma_s}^{\mu\mu} \sinh(y_s t / \tau_{B_s})}, \quad (3.12)$$

where ΔM_s denotes the mass difference between the heavy and light B_s mass eigenstates. The helicity eigenvalues of the muon pair are given by $\eta_L = +1$ and $\eta_R = -1$ for $\lambda = L$ and $\lambda = R$, respectively. Making use of eq. (3.6), the two CP observables $\mathcal{C}_{\mu\mu}^\lambda$ and $\mathcal{S}_{\mu\mu}$ can be written as

$$\mathcal{C}_{\mu\mu}^\lambda = -\eta_\lambda \frac{2|PS| \cos(\varphi_P - \varphi_S)}{|P|^2 + |S|^2} \equiv -\eta_\lambda \mathcal{C}_{\mu\mu}, \quad (3.13)$$

$$\mathcal{S}_{\mu\mu} = \frac{|P|^2 \sin 2\varphi_P - |S|^2 \sin 2\varphi_S}{|P|^2 + |S|^2}, \quad (3.14)$$

Input	Value	Unit	Ref.
τ_{B_s}	1.520 ± 0.005	10^{-12} s	[2]
$\Delta\Gamma_s/\Gamma_s$	0.127 ± 0.007		[2]
m_t^{pole}	172.57 ± 0.29	GeV	[2]
$m_b(m_b)$	4.183 ± 0.007	GeV	[2]
$m_s(m_s)$	93.5 ± 0.8	MeV	[2]
$f_{B_s} _{N_f=2+1+1}$	230.3 ± 1.3	MeV	[68]
$f_+^{K \rightarrow \pi}(0)$	0.9698 ± 0.0017		[68]
$ V_{us} f_+^{K \rightarrow \pi}(0)$	0.21635 ± 0.00038		[69, 70]
$ V_{ub} $	$3.86 \pm 0.07 \pm 0.12$	10^{-3}	[69]
$ V_{cb} $	$41.22 \pm 0.24 \pm 0.37$	10^{-3}	[69]
γ	$66.4_{-3.0}^{+2.8}$	$^\circ$	[71]

Table 1: Main input parameters used in our numerical analysis.

both of which are equal to zero in the SM, but lie between -1 and $+1$ in the presence of NP contributions. Summing eq. (3.12) over the muon helicities, we obtain the time-dependent rate asymmetry

$$\frac{\Gamma(B_s^0(t) \rightarrow \mu^+ \mu^-) - \Gamma(\bar{B}_s^0(t) \rightarrow \mu^+ \mu^-)}{\Gamma(B_s^0(t) \rightarrow \mu^+ \mu^-) + \Gamma(\bar{B}_s^0(t) \rightarrow \mu^+ \mu^-)} = \frac{\mathcal{S}_{\mu\mu} \sin(\Delta M_s t)}{\cosh(y_s t / \tau_{B_s}) + \mathcal{A}_{\Delta\Gamma_s}^{\mu\mu} \sinh(y_s t / \tau_{B_s})}. \quad (3.15)$$

Comparing the two CP-violating rate asymmetries defined by eqs. (3.12) and (3.15), we can see that the observables $\mathcal{A}_{\Delta\Gamma_s}^{\mu\mu}$ and $\mathcal{S}_{\mu\mu}$ can be extracted without measuring the muon helicity, while $\mathcal{C}_{\mu\mu}^\lambda$ is difficult to measure, since it requires the information of the muon helicity. It should be noted that the three observables $\mathcal{A}_{\Delta\Gamma_s}^{\mu\mu}$, $\mathcal{S}_{\mu\mu}$ and $\mathcal{C}_{\mu\mu}$ are not independent of each other, but satisfy the normalization relation

$$(\mathcal{A}_{\Delta\Gamma_s}^{\mu\mu})^2 + (\mathcal{S}_{\mu\mu})^2 + (\mathcal{C}_{\mu\mu}^\lambda)^2 = 1. \quad (3.16)$$

Therefore, we choose $\mathcal{A}_{\Delta\Gamma_s}^{\mu\mu}$ and $\mathcal{S}_{\mu\mu}$ as the two independent CP observables in the following analysis. They are also theoretically cleaner than the branching ratio, since their dependence on the decay constant f_{B_s} is cancelled.

In table 1, we list the main input parameters used in our numerical analysis. With these input values, our SM prediction of $\mathcal{B}(B_s \rightarrow \mu^+ \mu^-)$ has been already given in eq. (1.3).¹ Taking further into account the scalar S contribution (cf. eq. (3.3)),

¹For the input values of $|V_{ub}|$ and $|V_{cb}|$, we have adopted the CKMfitter average of the inclusive

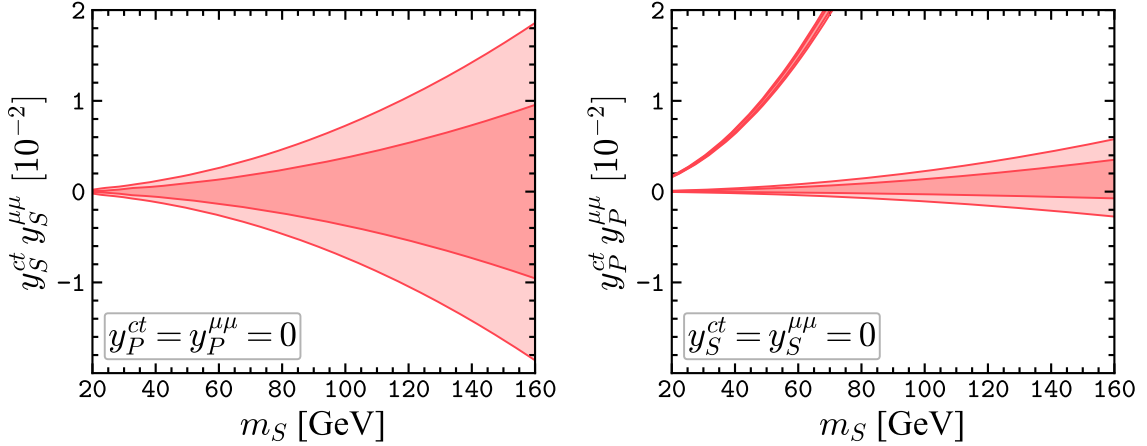


Figure 2: Constraints on $y_S^{ct} y_S^{\mu\mu}$ (left) and $y_P^{ct} y_P^{\mu\mu}$ (right) as a function of m_S from the $B_s \rightarrow \mu^+ \mu^-$ decay, in which $y_P^{ct} = y_P^{\mu\mu} = 0$ and $y_S^{ct} = y_S^{\mu\mu} = 0$ are assumed, respectively. The allowed regions at the 1σ and the 2σ confidence level (CL) are shown by the dark and the light red, respectively.

the branching ratio of $B_s \rightarrow \mu^+ \mu^-$ can be numerically written as²

$$\begin{aligned} \mathcal{B}(B_s \rightarrow \mu^+ \mu^-) \times 10^9 = & 3.51 - 3.34 \operatorname{Im} \left(\frac{y_P^{\mu\mu} y_R^{ct}}{0.01} \right) \left(\frac{100 \text{ GeV}}{m_S} \right)^2 \\ & + \left(0.79 \left| \frac{y_P^{\mu\mu} y_R^{ct}}{0.01} \right|^2 + 0.70 \left| \frac{y_S^{\mu\mu} y_R^{ct}}{0.01} \right|^2 \right) \left(\frac{100 \text{ GeV}}{m_S} \right)^4. \end{aligned} \quad (3.17)$$

It can be seen that the effects of the tcS couplings are largely enhanced compared to the SM contributions. This can be understood from the fact that the corresponding Wilson coefficients $\mathcal{C}_S^{\text{NP}}$ and $\mathcal{C}_P^{\text{NP}}$ contain a large CKM factor (cf. eq. (3.3)) and their contributions to the branching ratio do not suffer from the helicity suppression (cf. eqs. (3.5) and (3.6)). In addition, the difference between the coefficients of the $|y_P^{\mu\mu} y_R^{ct}|^2$ and $|y_S^{\mu\mu} y_R^{ct}|^2$ terms arise from the effects of $\mathcal{A}_{\Delta\Gamma_s}^{\mu\mu}$.

To illustrate the constraint from the measured branching ratio $\mathcal{B}(B_s \rightarrow \mu^+ \mu^-)$, we consider two simplified cases of $y_P^{ct} = y_P^{\mu\mu} = 0$ and $y_S^{ct} = y_S^{\mu\mu} = 0$, and show in figure 2 the allowed parameter regions in the $(m_S, y_S^{ct} y_S^{\mu\mu})$ and $(m_S, y_P^{ct} y_P^{\mu\mu})$ planes, respectively. In the former case, there exists only one allowed parameter region, since the NP contribution to \mathcal{C}_S has no linear interference with the dominant SM contribution $\mathcal{C}_{10}^{\text{SM}}$ and appears firstly at the quadratic order, as can be seen from eqs. (3.5) and (3.17). In the latter case, on the other hand, there exist two allowed

and exclusive determinations as given in table 1. When taking the inclusive (exclusive) values as input, the SM prediction becomes 5% higher (10% lower) than our prediction in eq. (1.3), which has only a minor impact on our subsequent numerical analysis of the NP effects. For more detailed discussions about the choices of $|V_{ub}|$ and $|V_{cb}|$, we refer to refs. [51, 72, 73].

²In order to present a compact numerical form, the correction from $\mathcal{A}_{\Delta\Gamma_s}^{\mu\mu}$ is calculated by taking $\varphi_S = \varphi_P = 0$. In our numerical analysis, however, the full analytical expressions are always used.

parameter regions: in the region with larger values of $y_P^{ct} y_P^{\mu\mu}$, the sign of the quantity P (cf. eq. (3.6)) is flipped by the large NP contribution to \mathcal{C}_P ; in the other region, the allowed values of $y_P^{ct} y_P^{\mu\mu}$ are much smaller and give a constructive interference with the dominant SM contribution $\mathcal{C}_{10}^{\text{SM}}$.

3.2 Muon $g - 2$

The muon anomalous magnetic moment $a_\mu = (g - 2)_\mu/2$ can provide powerful probes of NP effects [74, 75]. Taking into account the latest measurement by the Fermilab Muon $g - 2$ Experiment [76], the combined experimental average a_μ^{Exp} shows a 5.1σ discrepancy with the community-approved SM prediction $a_\mu^{\text{SM,WP}}$ from the Muon $g - 2$ Theory Initiative [75],

$$\Delta a_\mu^{\text{WP}} = a_\mu^{\text{Exp}} - a_\mu^{\text{SM,WP}} = (249 \pm 48) \times 10^{-11}, \quad (3.18)$$

which implies the presence of potential NP effects. For the SM prediction from the Muon $g - 2$ Theory Initiative [75], the hadronic vacuum polarization (HVP) contribution is evaluated by using the $e^+e^- \rightarrow$ hadrons cross sections measured by multiple experiments. However, a recent measurement of the $e^+e^- \rightarrow \pi^+\pi^-$ cross section from the CMD-3 experiment is found to be significantly higher than all the previous measurements [77, 78], which results in good consistency between a_μ^{Exp} and a_μ^{SM} . On the other hand, the lattice calculation of the HVP contribution by the BMW collaboration also disagrees significantly with the e^+e^- data [79], but goes in the same direction as the CMD-3 result. Recently, a new lattice calculation of the HVP contribution is performed in ref. [80], leading to

$$\Delta a_\mu^{\text{Lattice}} = a_\mu^{\text{Exp}} - a_\mu^{\text{SM,Lattice}} = (40 \pm 44) \times 10^{-11}, \quad (3.19)$$

which reduces the discrepancy to be only of 0.9 standard deviation. Although continued efforts are still needed to clarify the current theoretical situation [81], these recent evaluations of the HVP contribution also motivate us to consider the possibility of a good consistency between a_μ^{Exp} and a_μ^{SM} . Therefore, both Δa_μ^{WP} in eq. (3.18) and $\Delta a_\mu^{\text{Lattice}}$ in eq. (3.19) will be considered in our numerical analysis.

With the effective interactions given in eq. (2.2), the scalar S can shift a_μ by [82]

$$\Delta a_\mu^{\text{NP}} = \frac{1}{8\pi^2} \frac{m_\mu^2}{m_S^2} \left[(y_S^{\mu\mu})^2 \left(\ln \frac{m_S}{m_\mu} - \frac{7}{12} \right) + (y_P^{\mu\mu})^2 \left(-\ln \frac{m_S}{m_\mu} + \frac{11}{12} \right) \right], \quad (3.20)$$

in the regime $m_S \gg m_\mu$. In figure 3, the parameter regions in the $(y_S^{\mu\mu}, y_P^{\mu\mu})$ plane allowed to explain the $(g - 2)_\mu$ are shown for three benchmark masses $m_S = 20, 80$ and 140 GeV. Considering Δa_μ^{WP} in eq. (3.18), we can see that the coupling $y_S^{\mu\mu}$ should be nonzero, since the contribution related to $y_P^{\mu\mu}$ is always negative and thus increases the discrepancy of $(g - 2)_\mu$. Confronted with $\Delta a_\mu^{\text{Lattice}}$ in eq. (3.19), on the other hand, both $y_S^{\mu\mu}$ and $y_P^{\mu\mu}$ can be zero within the 2σ allowed regions.

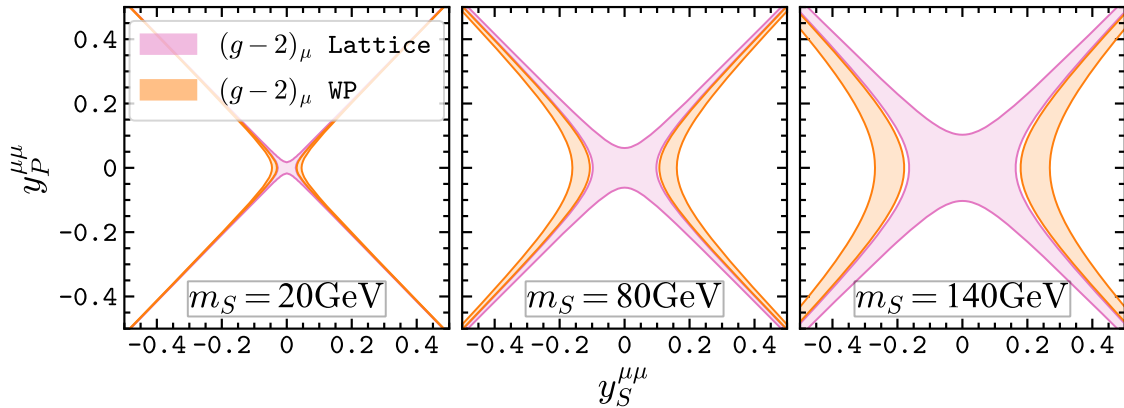


Figure 3: Constraints on $(y_S^{\mu\mu}, y_P^{\mu\mu})$ from the $(g-2)_\mu$ at the 2σ level, for three benchmark masses $m_S = 20, 80$ and 140 GeV. The orange and pink regions are allowed by considering eqs. (3.18) and (3.19), respectively.

3.3 Neutron EDM

The scalar singlet S with complex tcS couplings given in eq. (2.1) could also affect the hadronic EDM [83–85]. Generally, the low-energy effective Hamiltonian for the hadronic EDM takes the form [85]

$$\begin{aligned} \mathcal{H}_{\text{eff}} \supset &+ d_q(\mu) \cdot \frac{i}{2} \bar{q} \sigma^{\mu\nu} \gamma_5 q F_{\mu\nu} + \tilde{d}_q(\mu) \cdot \frac{i}{2} g_s(\mu) \bar{q} \sigma^{\mu\nu} T^a \gamma_5 q G_{\mu\nu}^a \\ &+ w(\mu) \cdot \frac{1}{3} f^{abc} G_{\mu\sigma}^a G_\nu^{b,\sigma} \tilde{G}^{c,\mu\nu}, \end{aligned} \quad (3.21)$$

where the index q runs over all quarks lighter than the top-quark mass m_t , and $g_s(\mu) = \sqrt{4\pi\alpha_s(\mu)}$ is the QCD gauge coupling. $F_{\mu\nu}$ and $G_{\mu\nu}^a$ denote the field-strength tensors of QED and QCD respectively, while $\tilde{G}^{a,\mu\nu} = \frac{1}{2} \epsilon^{\mu\nu\alpha\beta} G_{\alpha\beta}^a$ is the dual field-strength tensor of QCD, with the fully anti-symmetric Levi-Civita tensor $\epsilon^{\mu\nu\lambda\rho}$ defined with the convention $\epsilon^{0123} = +1$. T^a and f^{abc} are the generators and structure constants of the gauge group $SU(3)_C$, respectively.

The leading contribution to the charm-quark chromoelectric dipole moment (CEDM) \tilde{d}_c at the matching scale $\mu_t = \mathcal{O}(m_t)$ is obtained from the one-loop Feynman diagram shown on the left-hand side of figure 4. After integrating out the top quark and the scalar boson, it is straightforward to obtain [85–87]

$$\tilde{d}_c(\mu_t) = \frac{1}{32\pi^2} \frac{m_t}{m_S^2} f_1(x_{tS}) \text{Re}(y_S^{ct} y_P^{ct*}), \quad (3.22)$$

with $x_{tS} = m_t^2/m_S^2$ and the loop function

$$f_1(x) = \frac{x-3}{(x-1)^2} + \frac{2}{(x-1)^3} \ln x. \quad (3.23)$$

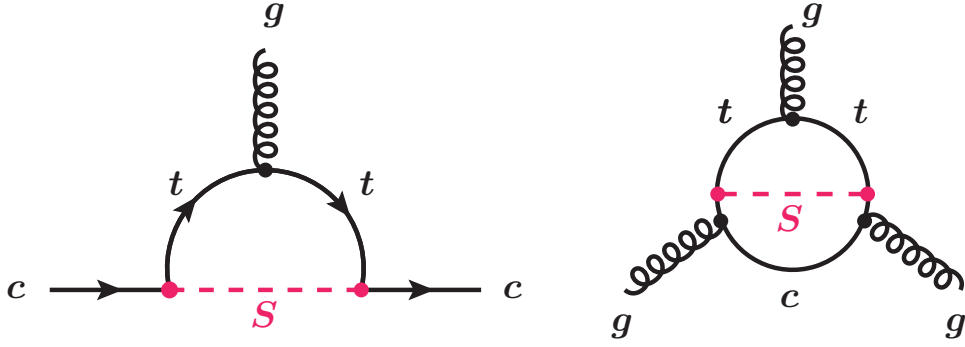


Figure 4: Left: One-loop Feynman diagram contributing to the CEDM of the charm quark. Right: Example of a two-loop Feynman diagram inducing the Weinberg operator. Both are due to the scalar singlet S with complex tcS couplings in eq. (2.1).

One can use the relation $\text{Re}(y_S^{ct}y_P^{ct*}) = \text{Im}(y_R^{ct}y_L^{ct*})/2$ to express eq. (3.22) in terms of y_R^{ct} and y_L^{ct} . The scalar singlet S can also contribute to the charm-quark EDM d_c through the same one-loop Feynman diagram in figure 4 but with the gluon replaced by a photon. As a result, one obtains $d_c(\mu_t) = Q_c e \tilde{d}_c(\mu_t)$, where $Q_c = +2/3$ is the charm-quark electric charge. The charm-quark EDM affects the neutron EDM through the flavour-mixing contributions into the down-quark EDM [88, 89] and mixing into the charm-quark CEDM under the QED Renormalization Group Evolution (RGE) [90, 91]. However, the contribution from d_c is found to be smaller than from \tilde{d}_c by at least one order of magnitude [90]. Therefore, the effect from the charm-quark EDM d_c can be safely neglected.

The matching condition $w(\mu_t)$ of the Weinberg operator is obtained by computing the two-loop Feynman diagrams in the full theory [92, 93], an example of which is displayed on the right-hand side of figure 4. Resorting to the results presented in refs. [85, 87] and setting the charm-quark mass to zero, we can write its explicit expression as

$$w(\mu_t) = \frac{g_s^3(\mu_t)}{(32\pi^2)^2} \frac{1}{m_S^2} f_2(x_{tS}) \text{Re}(y_S^{ct}y_P^{ct*}), \quad (3.24)$$

with the loop function given by

$$f_2(x) = -\frac{x^2 - 5x - 2}{3(x-1)^3} - \frac{2x}{(x-1)^4} \ln x. \quad (3.25)$$

We can also express eq. (3.24) in terms of y_R^{ct} and y_L^{ct} by making use of the relation $\text{Re}(y_S^{ct}y_P^{ct*}) = \text{Im}(y_R^{ct}y_L^{ct*})/2$.

The Wilson coefficients in the effective Hamiltonian of eq. (3.21) at the hadronic scale $\mu_H = 1 \text{ GeV}$ can be obtained by performing the necessary RGE [94]. In the

leading-logarithmic approximation, their numerical expressions are given by [85]

$$\begin{aligned}
\frac{d_d(\mu_H)}{e} &= 2.3 \times 10^{-8} \cdot \tilde{d}_c(\mu_t) + 1.0 \times 10^{-4} \text{ GeV} \cdot w(\mu_t), \\
\frac{d_u(\mu_H)}{e} &= -2.1 \times 10^{-8} \cdot \tilde{d}_c(\mu_t) - 9.1 \times 10^{-5} \text{ GeV} \cdot w(\mu_t), \\
\tilde{d}_d(\mu_H) &= 1.8 \times 10^{-6} \cdot \tilde{d}_c(\mu_t) + 7.0 \times 10^{-4} \text{ GeV} \cdot w(\mu_t), \\
\tilde{d}_u(\mu_H) &= 8.2 \times 10^{-7} \cdot \tilde{d}_c(\mu_t) + 3.1 \times 10^{-4} \text{ GeV} \cdot w(\mu_t), \\
w(\mu_H) &= 1.7 \times 10^{-2} \text{ GeV}^{-1} \cdot \tilde{d}_c(\mu_t) + 0.41 \cdot w(\mu_t).
\end{aligned} \tag{3.26}$$

It is noted that, under renormalization, the Weinberg operator mixes into the quark EDMs and CEDMs, but the opposite is not true. The appearance of the charm-quark CEDM \tilde{d}_c in the above equations is due to the charm-quark threshold correction to $w(\mu)$ at the scale $\mu = m_c$ [86, 95–97] and the subsequent RGE to the scale $\mu_H = 1 \text{ GeV}$. It can be seen that the RGE always tends to suppress these Wilson coefficients when running from a high down to a low scale.

In terms of the Wilson coefficients evaluated at the scale μ_H , the neutron EDM takes the following form [52]:

$$\begin{aligned}
\frac{d_n}{e} &= (1.0 \pm 0.5) \left\{ 1.4 \left[\frac{d_d(\mu_H)}{e} - 0.25 \frac{d_u(\mu_H)}{e} \right] + 1.1 \left[\tilde{d}_d(\mu_H) + 0.5 \tilde{d}_u(\mu_H) \right] \right\} \\
&\quad + (22 \pm 10) \times 10^{-3} \text{ GeV} \cdot w(\mu_H).
\end{aligned} \tag{3.27}$$

Plugging the results in eq. (3.26) into the above equation, we can express the neutron EDM in terms of the Wilson coefficients evaluated at the scale μ_t as

$$\left| \frac{d_n}{e} \right| = \left| (3.7 \pm 1.7) \times 10^{-4} \cdot \tilde{d}_c(\mu_t) + (9.3 \pm 4.1) \times 10^{-3} \text{ GeV} \cdot w(\mu_t) \right|. \tag{3.28}$$

As an illustration, taking $m_S = 100 \text{ GeV}$ and together with eqs. (3.22) and (3.24), this translates into

$$\left| \frac{d_n}{e} \right| = (1.11 \pm 0.51) \times 10^{-22} \text{ cm} \cdot |\text{Re}(y_S^{ct} y_P^{ct*})|. \tag{3.29}$$

The current 90% CL upper limit on the neutron EDM reads [98]

$$\left| \frac{d_n}{e} \right| < 1.8 \cdot 10^{-26} \text{ cm}. \tag{3.30}$$

We can use this limit to derive constraint on the tcS couplings, which is shown in figure 5. Here, to be conservative, we have set the numerical coefficients (1.0 ± 0.5) and (22 ± 10) in eq. (3.27) to 0.5 and 12, respectively. It can be seen that the upper bound on $|\text{Re}(y_S^{ct} y_P^{ct*})|$ or $|\text{Im}(y_R^{ct} y_L^{ct*})/2|$ is of the order of 10^{-4} and depends weakly on the scalar mass m_S .

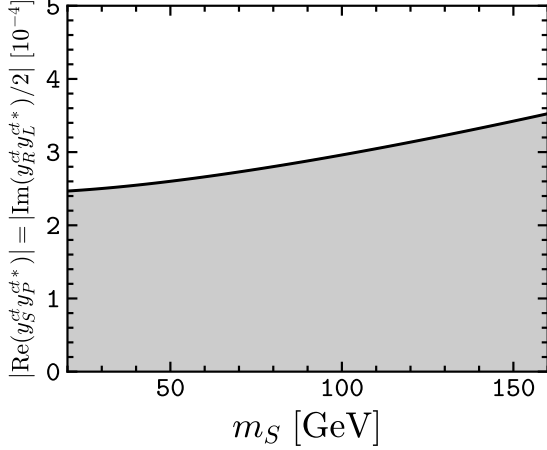
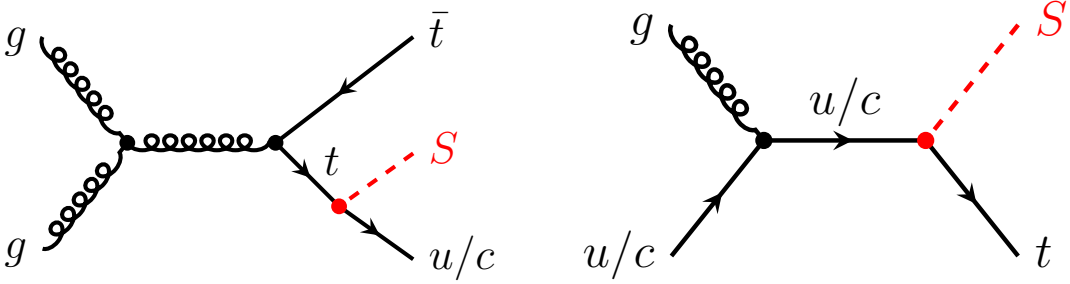


Figure 5: 90% CL upper bound on $|\text{Re}(y_S^{ct} y_P^{ct*})|$ or $|\text{Im}(y_R^{ct} y_L^{ct*})/2|$ as a function of m_S from the neutron EDM.



(a) $t\bar{t}$ production with one top decaying into qS . (b) single-top production associated with an S .

Figure 6: Representative Feynman diagrams for the production channels of the scalar S at the LHC, with its FCNC couplings to the top quark specified by eq. (2.1).

4 Phenomenology at the LHC

In this section, we investigate the collider signatures of the scalar singlet S introduced in section 2. According to its FCNC couplings to the top quark (cf. eq. (2.1)), the scalar S can be produced via the following two channels at the LHC: one is the top-pair production with one of the top quarks decaying into qS ($q = u, c$), and the other is the single-top production associated with a scalar S , i.e., $qg \rightarrow tS$. In figure 6, we show the corresponding Feynman diagrams, where the charge-conjugated processes are not shown but will be included in our numerical analysis. In subsections 4.1 and 4.2, we focus on the scenarios in which the scalar S decays to $\mu^+ \mu^-$ and $b\bar{b}$ pair, respectively. The scenario in which both of the two decay channels are involved will be considered in subsection 4.3. In addition, since the processes we are considering are not sensitive to the difference between the couplings y_S^{ct} and y_P^{ct} , we can take, for simplicity, $y_P^{ct} = 0$ in the following analysis.

	Top pair			Single top			Others	
	tt	$t\bar{t}bb$	$t\bar{t}V$	tj	tW	tb	tZ	VV
K -factor	1.6	1.25	1.3	1.2	1.3	1.5	1.6	1.7
Refs.	[107, 108]	[109]	[110]	[111]	[111]	[111]	[112]	[113]

Table 2: The K -factors for the different background channels.

In our numerical analysis, the signal and the SM background events are simulated with `MadGraph5` [99]. Dedicated Universal FeynRules Output (UFO) [100] model files are produced with `FeynRules` [101]. Then, `Pythia8` [102] is used to simulate the parton shower and hadronization, and `Delphes` [103] is used to simulate the detector effects with the default CMS card, in which the anti- k_t algorithm [104] is chosen for clustering the jets with radius parameter $\Delta R = 0.4$. Finally, the detector-level samples are analyzed with the `MadAnalysis5` [105]. In addition, we use the NNPDF2.3 [106] leading-order parton distribution functions during our calculation.

The generated signal events for the top-pair production channel are normalized by using the NNLO+NNLL theoretical prediction $\sigma(pp \rightarrow t\bar{t}) = 984.5$ pb at $\sqrt{s} = 14$ TeV [107] and the experimental measurement $\mathcal{B}(t \rightarrow b\ell\nu_\ell) = 0.225$ with $\ell = e, \mu$ [2], while the cross section for $pp \rightarrow tS$ channel is calculated at the leading order in QCD. In order to include the higher-order QCD corrections for the background channels, the simulated samples generated at the leading order are scaled by the K -factors, which are defined as the ratio of the higher- and the leading-order cross-sections calculated. For convenience, their values are listed in table 2 for the different background channels.

In order to obtain the upper limits on the signal cross-sections, we adopt the statistical significance defined in ref. [114]

$$Z = \sqrt{2 \left[(S + B) \ln \left(1 + \frac{S}{B} \right) - S \right]}, \quad (4.1)$$

where S and B denote the total event numbers in a specific phase-space region of the signal and background channels, respectively. They can be evaluated by $\mathcal{L} \times \sigma \times \mathcal{B} \times \varepsilon$, in which \mathcal{L} is the integrated luminosity, and σ and \mathcal{B} denote the cross section and the decay branching fraction of a specific channel, respectively. ε represents the cut efficiency for a specific signal region, which will be studied in detail for the decay channels $S \rightarrow \mu^+\mu^-$ and $S \rightarrow b\bar{b}$ in subsection 4.1 and 4.2, respectively.

4.1 Three-lepton final states through $S \rightarrow \mu^+ \mu^-$ channel

In this subsection, we focus on the scenario in which the scalar S decays into a pair of muons. For the two production channels shown in figure 6, we consider the following decay chains:

$$\begin{aligned} pp &\rightarrow t(\rightarrow b\ell\nu_\ell)t(\rightarrow qS, S \rightarrow \mu^+\mu^-) && \rightarrow 3\ell + 1b + 1j + \cancel{E}_T, \\ pp &\rightarrow t(\rightarrow b\ell\nu_\ell)S(\rightarrow \mu^+\mu^-) && \rightarrow 3\ell + 1b + \cancel{E}_T, \end{aligned}$$

where b and j denote the b -tagged and the light jet, while \cancel{E}_T is the missing transverse energy. The signal contains exactly three isolated leptons (two of them are muons with opposite charges), at least one jet (one is the b -tagged jet), and missing transverse energy.

The same signature can also arise from multiple SM backgrounds. Here we consider only the most significant ones arising from $t\bar{t}$, $t\bar{t}V$, tZ , VV and tW , with $V = W, Z$, together with their detailed decay chains given by

$$\begin{aligned} t\bar{t} &: \quad pp \rightarrow t(\rightarrow b\ell\nu_\ell)\bar{t}(\rightarrow \bar{b}\ell\bar{\nu}_i) && \rightarrow 2\ell + 2b + \cancel{E}_T, \\ t\bar{t}V &: \quad pp \rightarrow t(\rightarrow b\ell\nu_\ell)\bar{t}(\rightarrow \bar{b}\ell\bar{\nu}_i)V(\rightarrow \ell + \ell/\nu_\ell) && \rightarrow 3-4\ell + 2b + \cancel{E}_T, \\ tZ &: \quad pp \rightarrow t(\rightarrow b\ell\nu_\ell)Z(\rightarrow \ell\ell)j && \rightarrow 3\ell + 1b + 1j + \cancel{E}_T, \\ VV &: \quad pp \rightarrow VV(\rightarrow \ell + \ell/\nu_\ell) && \rightarrow 2-4\ell + \cancel{E}_T, \\ tW &: \quad pp \rightarrow t(\rightarrow b\ell\nu_\ell)W(\rightarrow \ell\nu_\ell) && \rightarrow 2\ell + 1b + \cancel{E}_T, \end{aligned}$$

where the CP-conjugated processes are self-evident.

The simulated signal and background samples are generated following the steps described above. Furthermore, the following fiducial phase-space selections at the parton level are imposed:

$$p_T^j > 20 \text{ GeV}, \quad p_T^\ell > 10 \text{ GeV}, \quad |\eta^j| < 5, \quad |\eta^\ell| < 2.5, \quad \Delta R(m, n) > 0.4 \quad (m, n = \ell, b, j), \quad (4.2)$$

where p_T and η denote the transverse momentum and the pseudo-rapidity, respectively. $\Delta R(m, n) = \sqrt{(\Delta\eta)^2 + (\Delta\phi)^2}$ denotes the separation between the particles m and n in the $\eta - \phi$ plane. In addition, since the values of tcS couplings do not affect the distributions of final states, we take $y_S^{ct} = 0.001$ for the signal sample simulation.

At the detector level, the jets are required to have $p_T > 25 \text{ GeV}$ and $|\eta| < 2.5$, while the leptons should have $p_T > 15 \text{ GeV}$ and $|\eta| < 2.5$ and at least one lepton is required to have $p_T > 25 \text{ GeV}$ to satisfy the trigger threshold. With these prerequisites, we select signals by further requiring the events to contain exactly three isolated leptons (two of them are muons with opposite charges), at least one light jet, and exactly one b -tagged jet.

In order to further reduce the SM backgrounds, we also require a full reconstruction of the scalar singlet S and the spectator top quark. To this end, the scalar

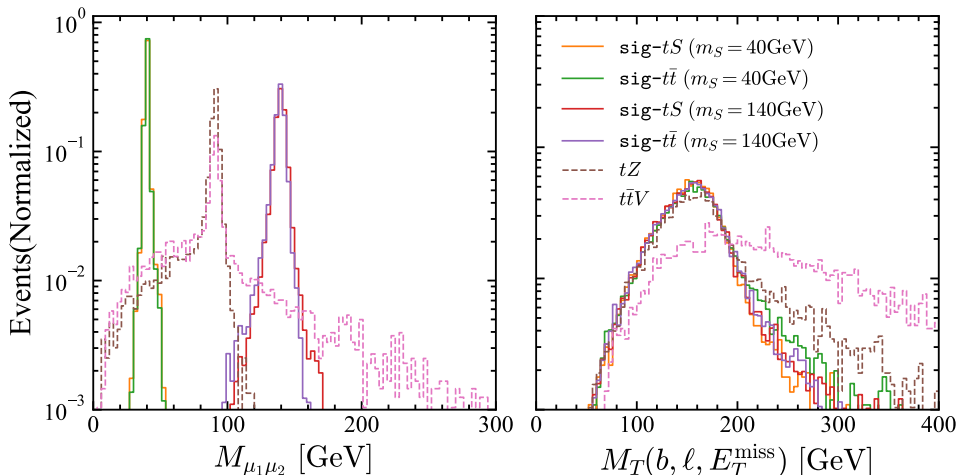


Figure 7: $M_{\mu_1\mu_2}$ (left) and $M_T(b, \ell, \cancel{E}_T)$ (right) distributions for the signal with two benchmark masses $m_S = 40$ GeV and 140 GeV as well as for the two dominant backgrounds $t\bar{t}V$ and tZ , where the basic and the multiplicity cut have been imposed.

resonance S is reconstructed from the invariant mass $M_{\mu_1\mu_2}$ of an opposite-sign muon pair (marked as μ_1, μ_2).³ Then, the remaining lepton (ℓ), combined with the b -tagged jet and the missing transverse energy, is used to reconstruct the transverse mass of the spectator top quark, with [2]

$$M_T(b, \ell, \cancel{E}_T) = \sqrt{(E_{T,b\ell} + \cancel{E}_T)^2 - (\vec{p}_{T,b\ell} + \vec{\cancel{p}}_T)^2}, \quad (4.3)$$

where the missing transverse momentum $\vec{\cancel{p}}_T$ is reconstructed as the negative vector sum of the transverse momenta of all the visible final states, and the missing transverse energy is defined as $\cancel{E}_T = |\vec{\cancel{p}}_T|$. For the $b - \ell$ system, its transverse momentum and transverse energy are defined, respectively, as $\vec{p}_{T,b\ell} = \vec{p}_{T,b} + \vec{p}_{T,\ell}$ and $E_{T,b\ell} = \sqrt{|\vec{p}_{T,b\ell}|^2 + M_{b\ell}^2}$, with the invariant mass $M_{b\ell}^2 = (p_b + p_\ell)^2$. In figure 7, we show the distributions of $M_{\mu_1\mu_2}$ and $M_T(b, \ell, \cancel{E}_T)$ for the signals with two benchmark points $m_S = 40$ GeV and 140 GeV as well as for the two dominant backgrounds $t\bar{t}V$ and tZ . It can be seen that the $M_{\mu_1\mu_2}$ distributions of the signal channels have peaks at the corresponding m_S . However, the peaks for the backgrounds appear at m_Z . In addition, as expected, the $M_T(b, \ell, \cancel{E}_T)$ distributions have an end-point at m_t .

According to the above analysis, we require the invariant mass $M_{\mu_1\mu_2}$ to lie in the regime of ± 20 GeV around the input m_S , while the reconstructed transverse masses $M_T(b, \ell, \cancel{E}_T)$ are required to satisfy a loose requirement, being less than 200 GeV.

³If an event contains more than one pair of qualified muons, the pair with an invariant mass closer to the input m_S will be selected. In this way, the $M_{\mu_1\mu_2}$ distributions of the backgrounds depend on the prior m_S . However, our numerical results show that the differences of the distributions caused by the different m_S values are insignificant.

m_S	20 GeV	40 GeV	60 GeV	80 GeV	100 GeV	120 GeV	140 GeV	160 GeV
init	42.15(1.72)	38.76(1.53)	33.47(1.30)	26.69(1.10)	19.13(0.92)	11.61(0.77)	5.20(0.64)	1.07(0.54)
cut-1	36.49(1.49)	34.47(1.36)	30.40(1.20)	24.64(1.03)	17.83(0.87)	10.88(0.73)	4.91(0.62)	1.03(0.52)
cut-2	4.14(0.12)	3.98(0.11)	3.70(0.11)	3.18(0.10)	2.40(0.09)	1.42(0.08)	0.59(0.07)	0.12(0.06)
cut-3	3.50(0.11)	3.38(0.10)	3.17(0.10)	2.73(0.09)	2.06(0.08)	1.22(0.07)	0.51(0.06)	0.09(0.05)
Eff. [%]	8.30(6.09)	8.72(6.71)	9.47(7.37)	10.22(8.19)	10.77(8.63)	10.54(9.00)	9.87(9.33)	8.76(9.43)

Table 3: Event yields of $t\bar{t}$ (tS) production channels for eight benchmark values of m_S with $y_S^{ct} = 0.001$, assuming an integrated luminosity of 150 fb^{-1} and a centre-of-mass energy of $\sqrt{s} = 14 \text{ TeV}$. The last line gives the accumulated efficiencies after the three cuts.

cut	init	cut-1	cut-2	cut-3							
				20 GeV	40 GeV	60 GeV	80 GeV	100 GeV	120 GeV	140 GeV	160 GeV
$t\bar{t}$	1031746	841756	126.39	18.06	30.95	25.79	23.21	20.63	20.63	20.63	20.63
$t\bar{t}V$	923	836	45.45	1.39	3.04	4.37	10.89	11.14	3.95	3.14	2.31
tW	595703	475172	1.99	0.00	1.99	1.99	0.00	0.00	0.00	0.00	0.00
tZ	2952	2619	160.11	5.07	9.82	15.97	128.01	129.28	12.91	6.95	5.07
VV	972368	673783	145.86	4.86	19.45	19.45	87.51	92.37	9.72	4.86	4.86
VVV	76	72	0.30	0.01	0.01	0.02	0.07	0.06	0.01	0.01	0.01

Table 4: Event yields for different backgrounds after each cut, assuming an integrated luminosity of 150 fb^{-1} and a centre-of-mass energy of $\sqrt{s} = 14 \text{ TeV}$.

The selection criterion on $M_{\mu_1\mu_2}$ means that we need to define the signal regions depending on the prior m_S values. Finally, we summarize the cuts at the detector level as follows:

cut-1: basic cut with $p_T^\ell > 15 \text{ GeV}$, $p_T^j > 25 \text{ GeV}$, $|\eta^{\ell,j}| < 2.5$, $\max(p_T^\ell) > 25 \text{ GeV}$,

cut-2: multiplicity cut with $N(\ell) = 3$, $N(\mu^+\mu^-) \geq 1$, $N(j) \geq 1$, $N(b) = 1$,

cut-3: invariant mass cut with $|M_{\mu_1\mu_2} - m_S| < 20 \text{ GeV}$, $M_T(b, \ell, \cancel{E}_T) < 200 \text{ GeV}$.

The cut flows for the signals with several benchmark values of m_S and the SM backgrounds are shown in tables 3 and 4, respectively. Here we consider an integrated luminosity of 150 fb^{-1} and a centre-of-mass energy of $\sqrt{s} = 14 \text{ TeV}$.

The expected upper bounds on the parameters m_S and y_S^{ct} are derived by using the statistical significance Z defined in eq. (4.1), where S and B denote the event numbers after all the three cuts for the signals and backgrounds, respectively. For the integrated luminosities of $\mathcal{L} = 150 \text{ fb}^{-1}$ and 3000 fb^{-1} , the expected 95% upper bounds on $|y_S^{ct}|$ for several benchmark values of m_S are shown in figure 8. By using

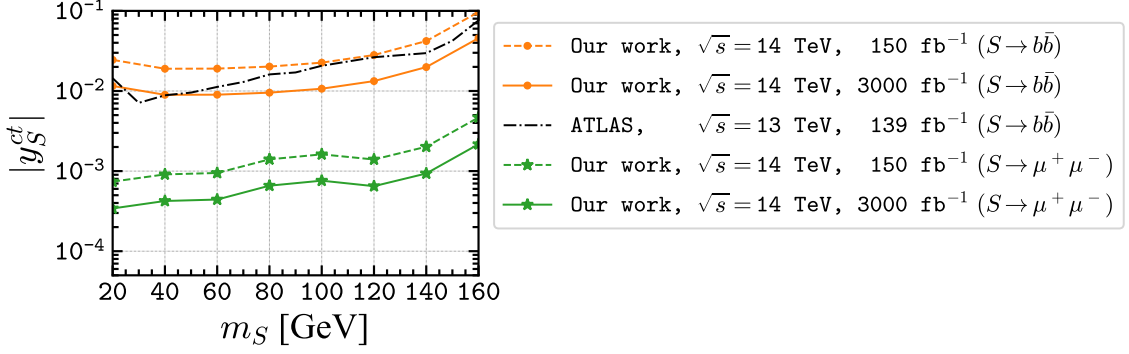


Figure 8: The expected 95% CL upper bounds on $|y_S^{ct}|$ in the $\mu^+\mu^-$ and $b\bar{b}$ channels, assuming $\mathcal{B}(S \rightarrow \mu^+\mu^-) = 100\%$ and $\mathcal{B}(S \rightarrow b\bar{b}) = 100\%$, respectively. The bounds are obtained for $\mathcal{L} = 150 \text{ fb}^{-1}$ (dashed line) and 3000 fb^{-1} (solid line). The ATLAS bound from a search of $t \rightarrow qX$, with $X \rightarrow b\bar{b}$, produced in $t\bar{t}$ events based on $\mathcal{L} = 139 \text{ fb}^{-1}$ [23] is also shown (gray dashed line).

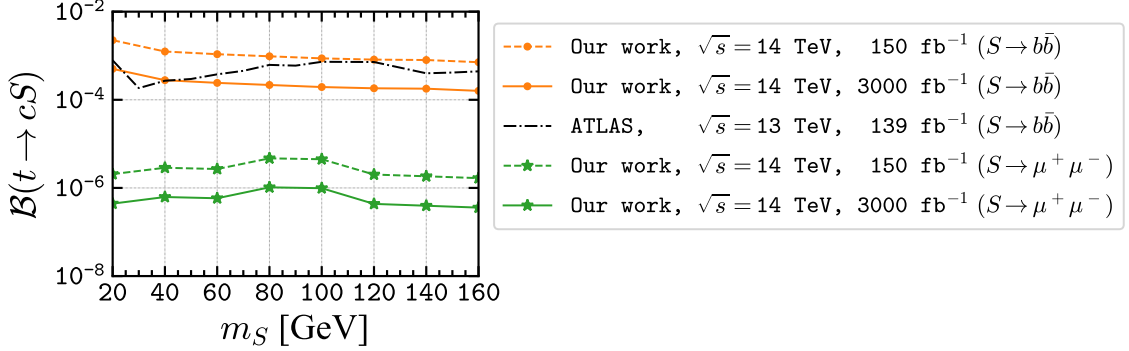


Figure 9: The expected 95% CL upper bounds on the branching ratio of $t \rightarrow cS$ decay, which is derived by using the expected bounds on $|y_S^{ct}|$ shown in figure 8. The other captions are the same as in figure 8.

eq. (2.4), we can then derive the corresponding upper bounds on the branching ratio $\mathcal{B}(t \rightarrow cS)$, which are shown in figure 9. For $\mathcal{L} = 150 \text{ fb}^{-1}$ with $\sqrt{s} = 14 \text{ TeV}$, our results are consistent with the analysis for the 13 TeV LHC in ref. [22].

4.2 Three- b -jet final states through $S \rightarrow b\bar{b}$ channel

In this subsection, we focus on the scenario in which the scalar S decays to $b\bar{b}$ after the production, as shown in figure 6. The full decay chains can be written as

$$\begin{aligned}
 pp \rightarrow t(\rightarrow b\ell\nu_\ell)t(\rightarrow qS, S \rightarrow b\bar{b}) &\rightarrow \geq 1j + 3b + 1\ell + \cancel{E}_T, \\
 pp \rightarrow t(\rightarrow b\ell\nu_\ell)S(\rightarrow b\bar{b}) &\rightarrow \geq 0j + 3b + 1\ell + \cancel{E}_T.
 \end{aligned}$$

The signals are characterized by at least three jets (three of them are b -tagged), exactly one isolated lepton, and missing transverse energy.

m_S	20 GeV	40 GeV	60 GeV	80 GeV	100 GeV	120 GeV	140 GeV	160 GeV
init	42.51(1.74)	38.92(1.53)	33.24(1.30)	26.15(1.09)	18.45(0.91)	11.10(0.76)	5.07(0.63)	1.30(0.53)
cut-1	23.71(1.02)	21.48(0.89)	18.24(0.75)	14.34(0.62)	10.11(0.52)	6.06(0.43)	2.78(0.35)	0.71(0.30)
cut-2	1.55(0.02)	2.28(0.05)	2.24(0.07)	1.94(0.07)	1.52(0.07)	0.97(0.06)	0.46(0.06)	0.12(0.05)
cut-3	0.87(0.01)	1.44(0.03)	1.42(0.03)	1.24(0.04)	0.97(0.04)	0.62(0.03)	0.28(0.03)	0.07(0.03)
Eff. [%]	2.06(0.64)	3.71(1.65)	4.26(2.64)	4.75(3.32)	5.27(3.92)	5.59(4.56)	5.59(4.97)	5.28(5.41)

Table 5: Same as in table 3, but for the signal channel with three- b -jet final states.

For this channel, the dominant background is expected to come from $t\bar{t}$ production associated with two additional jets. Due to the potential misidentification of light jets as the b -tagged jets, the single top and the single gauge boson production with two b -jets are also included. All the backgrounds considered are summarized as

$$\begin{aligned}
t\bar{t}jj &: pp \rightarrow t(\rightarrow bj\bar{j})\bar{t}(\rightarrow \bar{b}\ell\bar{\nu}_\ell) & \rightarrow & \geq 2j + 2b + 1\ell + \cancel{E}_T, \\
t\bar{t}bb &: pp \rightarrow t(\rightarrow bj\bar{j})\bar{t}(\rightarrow \bar{b}\ell\bar{\nu}_\ell) + bb & \rightarrow & \geq 2j + 4b + 1\ell + \cancel{E}_T, \\
tW &: pp \rightarrow t(\rightarrow bj\bar{j})W(\rightarrow \ell\nu_\ell) & \rightarrow & \geq 2j + b + 1\ell + \cancel{E}_T, \\
tb \text{ (s-channel)} &: pp \rightarrow t(\rightarrow b\ell\nu_\ell) + b & \rightarrow & \geq 0j + 2b + 1\ell + \cancel{E}_T, \\
tb \text{ (t-channel)} &: pp \rightarrow t(\rightarrow b\ell\nu_\ell) + j & \rightarrow & \geq 1j + 1b + 1\ell + \cancel{E}_T, \\
Wbb &: pp \rightarrow W(\rightarrow \ell\nu_\ell) + bb & \rightarrow & 2b + 1\ell + \cancel{E}_T, \\
Zbb &: pp \rightarrow Z(\rightarrow \ell\ell) + bb & \rightarrow & 2b + 2\ell.
\end{aligned}$$

For the $t\bar{t}jj$, Wbb and Zbb channels, the samples are merged up to two extra light jets, while the samples of the tW channel are merged up to one extra light jet.

Both signal and background events are simulated and analyzed by using the same method as in the last subsection. Furthermore, at the detector level, we require the jets to have $p_T^j > 25$ GeV and $|\eta^j| < 2.5$, and the leptons to have $p_T^\ell > 15$ GeV and $|\eta^\ell| < 2.5$. The events are also required to fulfill the following selection criteria:

cut-1: $N(\ell) = 1$, i.e., exactly one isolated lepton (e^\pm or μ^\pm),

cut-2: $N(b) = 3$, i.e., exactly three b -tagged jets,

cut-3: $N(j) = 1$ or 2 , i.e., one or two additional light jets.

For an integrated luminosity of 150 fb^{-1} , the above cut flows for the signals with several benchmark values of m_S and the backgrounds are shown in tables 5 and 6, respectively.

As in the last subsection, these results can be interpreted as the expected bounds on the couplings and mass of the scalar singlet S . For integrated luminosities of $\mathcal{L} = 150 \text{ fb}^{-1}$ and 3000 fb^{-1} at the LHC with $\sqrt{s} = 14$ TeV, the expected 95% upper

	$t\bar{t}jj$	$t\bar{t}bb$	Wbb	tW	Zbb	tb (t-channel)	tb (s-channel)
init	34520720	705553	42821826	10865010	12762239	31941000	1511010
cut-1	18448881	377605	20204002	2597650	5573320	4483686	185839
cut-2	3543108	102256	493736	163866	117192	107769	8398
cut-3	1782085	58575	329158	101392	65298	50275	3512

Table 6: Event yields for the backgrounds after each cut, assuming $\mathcal{L} = 150 \text{ fb}^{-1}$.

bounds on $|y_S^{ct}|$ for several benchmark values of m_S are shown in figure 8, and the corresponding upper limits on $\mathcal{B}(t \rightarrow cS)$ are shown in figure 9. For comparison, the ATLAS bound from the search of $t \rightarrow qX$, with $X \rightarrow b\bar{b}$, produced in $t\bar{t}$ events is also shown, which is based on the Run 2 dataset corresponding to an integrated luminosity of 139 fb^{-1} at $\sqrt{s} = 13 \text{ TeV}$ [23]. For $\mathcal{L} = 3000 \text{ fb}^{-1}$ with $\sqrt{s} = 14 \text{ TeV}$, our results are consistent with the analysis in ref. [21].

4.3 Multiple final states

The discussions in the last two subsections assume that only one decay channel of the scalar singlet S dominates each time. However, the $b\bar{b}$ and $\mu^+\mu^-$ decay channels could exist simultaneously. Then, according to eq. (2.3), the branching ratio of the $\mu^+\mu^-$ channel can be written as

$$\mathcal{B}(S \rightarrow \mu^+\mu^-) = \frac{\beta_\mu^3}{\beta_\mu^3 + 3R^2\beta_b^3}, \quad (4.4)$$

with the ratio $R \equiv y_S^{bb}/y_S^{\mu\mu}$, and $\mathcal{B}(S \rightarrow b\bar{b}) = 1 - \mathcal{B}(S \rightarrow \mu^+\mu^-)$. Therefore, the sensitivities to the tcS couplings from the LHC direct searches depend on the ratio R . In figure 10, the expected upper bounds on $|y_S^{ct}|$ from the $\mu^+\mu^-$ and $b\bar{b}$ channels are shown as a function of R . For $R \lesssim 10$, we can see that the expected upper bounds from the $\mu^+\mu^-$ channel are stronger than from the $b\bar{b}$ channel. In figure 10, we also show the resulting branching ratios $\mathcal{B}(S \rightarrow \mu^+\mu^-)$ for different values of R .⁴ In a more realistic situation, the scalar singlet S can even have other decay channels, such as the $\gamma\gamma$ and $\tau^+\tau^-$ modes. In this case, considering the $\mu^+\mu^-$ channel, the expected bound for a given value of $\mathcal{B}(S \rightarrow \mu^+\mu^-)$ is equivalent to that for the corresponding R value shown in figure 10. For example, the bounds obtained by assuming $\mathcal{B}(S \rightarrow \mu^+\mu^-) = 100\%$, 31% and 0.44% are equivalent to the results for $R = 0$, 1 and 10 in figure 10, respectively.

⁴For $m_S > 20 \text{ GeV}$, the branching ratio $\mathcal{B}(S \rightarrow \mu^+\mu^-)$ shows a very weak dependence on the scalar mass m_S . Therefore, $m_S = 20 \text{ GeV}$ is taken in the evaluation of $\mathcal{B}(S \rightarrow \mu^+\mu^-)$.

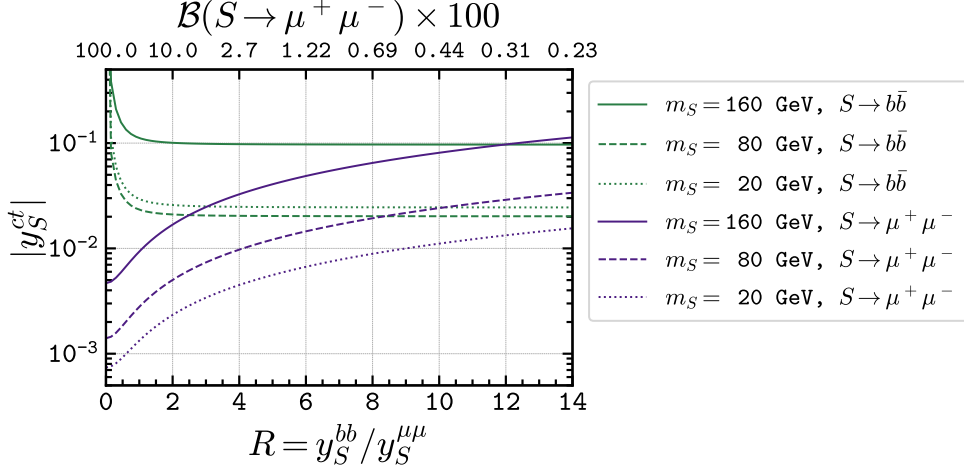


Figure 10: The expected 95% CL upper bounds on $|y_S^{ct}|$ as a function of $R = y_S^{bb}/y_S^{\mu\mu}$ for $m_S = 20, 80$ and 160 GeV. The green and purple curves correspond to the bounds obtained in the $b\bar{b}$ and $\mu^+\mu^-$ channels with $\mathcal{L} = 150 \text{ fb}^{-1}$, respectively. The branching ratios $\mathcal{B}(S \rightarrow \mu^+\mu^-)$ for different values of R are also given in the upper axis.

5 Combined analysis

In this section, we perform a combined analysis under the constraints derived in the previous sections. The tcS couplings are assumed to be CP-conserving and CP-violating in the following two subsections, respectively.

5.1 CP-conserving tcS couplings

With our specification for the couplings of the scalar singlet S with the SM fermions (cf. eqs. (2.1) and (2.2)), there involve totally six free coupling parameters y_S^{ct} , y_P^{ct} , $y_S^{\mu\mu}$, $y_P^{\mu\mu}$, y_S^{bb} , and y_P^{bb} . Since all the observables considered are not sensitive to the difference between y_S^{bb} and y_P^{bb} , we take $y_P^{bb} = 0$ without loss of generality. For the $B_s \rightarrow \mu^+\mu^-$ decay, the NP contribution involves only the combination $y_S^{ct} + iy_P^{ct} \equiv y_R^{ct}$ (cf. eq. (3.3)), which is real for the CP-conserving tcS interaction. Therefore, it is convenient to use the chiral basis, i.e., y_L^{ct} and y_R^{ct} . Since these two couplings are added quadratically in the branching ratio of $t \rightarrow cS$ decay (cf. eq. (2.4)), the upper bound on $|y_R^{ct}|$ from the LHC direct searches can be obtained by setting $y_L^{ct} = 0$ and vice versa. Therefore, we are left with only the four coupling parameters y_R^{ct} , $y_S^{\mu\mu}$, $y_P^{\mu\mu}$, and y_S^{bb} . For the first three ones, we consider the following two scenarios:

$$(y_R^{ct}, y_S^{\mu\mu}, y_P^{\mu\mu}) = \begin{cases} (\times, \times, 0) & \text{scenario S1,} \\ (\times, 0, \times) & \text{scenario P1,} \end{cases} \quad (5.1)$$

where \times denotes a nonzero entry. For each scenario, several typical benchmark values of $y_S^{bb}/y_{S,P}^{\mu\mu}$ and m_S will be considered. It is noted that CP is conserved in

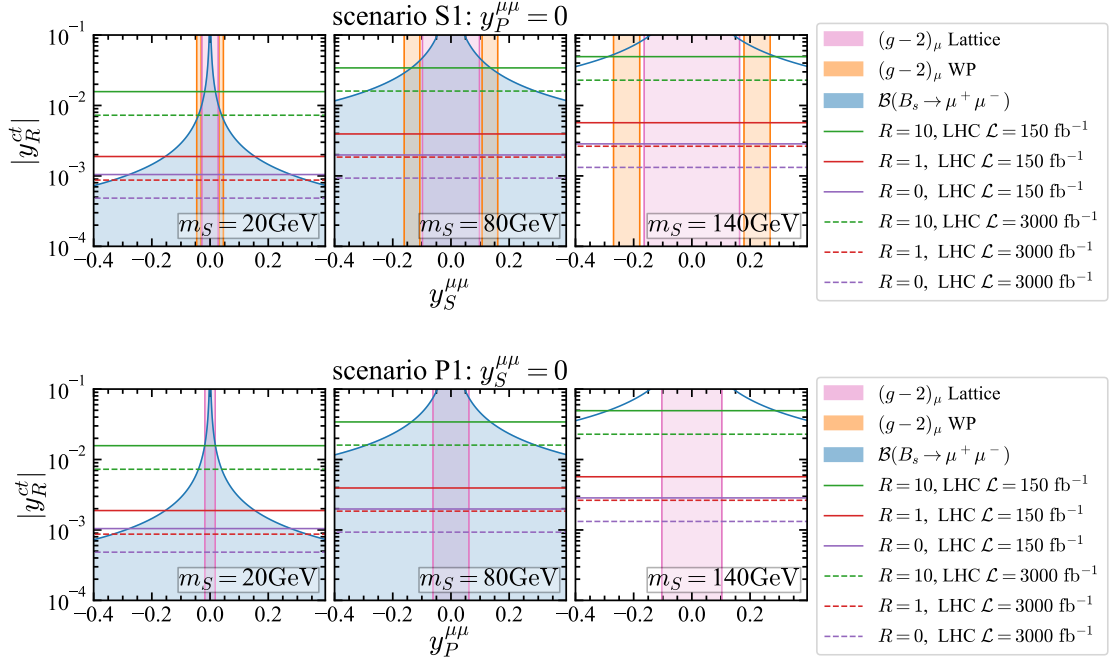


Figure 11: Constraints on the couplings $(y_R^{ct}, y_S^{\mu\mu})$ in scenario S1 and on $(y_R^{ct}, y_P^{\mu\mu})$ in scenario P1. The 2σ allowed regions by the branching ratio $\mathcal{B}(B_s \rightarrow \mu^+ \mu^-)$ and the $(g-2)_\mu$ from eq. (3.18) (eq. (3.19)) are shown by blue and orange (pink), respectively. For each $R = y_S^{bb}/y_{S,P}^{\mu\mu}$ value, the expected 95% CL upper bounds at the LHC with 150 fb^{-1} and 3000 fb^{-1} are shown by the horizontal lines.

both the quark and lepton sectors in scenario S1, but violated in the lepton sector in scenario P1.

In each scenario, we consider the constraints from the $B_s \rightarrow \mu^+ \mu^-$ decay, $(g-2)_\mu$, and the direct searches at the LHC with the decay channel $S \rightarrow \mu^+ \mu^-$. For the benchmark masses $m_S = 20, 80$ and 140 GeV , the allowed parameter spaces of $(y_R^{ct}, y_{S,P}^{\mu\mu})$ are shown in figure 11. From this figure, we make the following observations:

- In scenario S1, considering the SM prediction from the Muon $g-2$ Theory Initiative [75], the $(g-2)_\mu$ can be explained by a nonzero scalar coupling $y_S^{\mu\mu}$. In figure 11, we also show the constraints by considering the recent lattice result for the HVP contribution in ref. [80]. In the allowed parameter regions of $y_S^{\mu\mu}$ corresponding to the two SM predictions of $(g-2)_\mu$, we can see that the upper bounds from the $B_s \rightarrow \mu^+ \mu^-$ decay are weaker than the expected 95% CL upper bounds at the LHC for $R \lesssim 5$.
- In scenario P1, the main difference from scenario S1 is the constraint from $(g-2)_\mu$. Considering the SM prediction from the Muon $g-2$ Theory Initiative [75], the $(g-2)_\mu$ cannot be explained by the coupling $y_P^{\mu\mu}$ in this scenario. Therefore, we show in figure 11 only the constraints from the recent lattice result for the

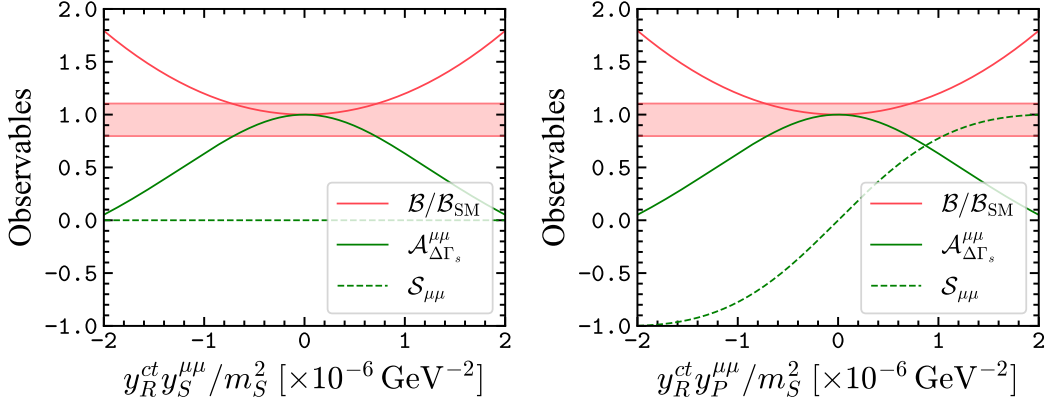


Figure 12: The predicted $\mathcal{B}/\mathcal{B}_{\text{SM}}$, $\mathcal{A}_{\Delta\Gamma_s}^{\mu\mu}$ and $\mathcal{S}_{\mu\mu}$ of the $B_s \rightarrow \mu^+\mu^-$ decay as a function of $y_R^{\text{ct}}y_S^{\mu\mu}/m_S^2$ in scenario S1 (left) and $y_R^{\text{ct}}y_P^{\mu\mu}/m_S^2$ in scenario P1 (right). The red band denotes the 2σ range of $\mathcal{B}_{\text{exp}}/\mathcal{B}_{\text{SM}}$ obtained from eqs. (1.2) and (1.3).

HVP contribution in ref. [80]. For the $B_s \rightarrow \mu^+\mu^-$ decay, the constraints in this scenario are almost identical to the ones in scenario S1, which can be understood from the semi-numerical result in eq. (3.17), keeping in mind that y_R^{ct} is real for CP-conserving tcS interaction. In addition, we find that the allowed regions by both the $B_s \rightarrow \mu^+\mu^-$ and $(g-2)_\mu$ are weaker than the expected 95% CL upper bounds at the LHC for $R \lesssim 10$.

- For these two scenarios, the upper bounds on the tcS couplings from the $B_s \rightarrow \mu^+\mu^-$ decay relative to the expected bounds at the LHC become stronger for lighter scalar S .

For the $B_s \rightarrow \mu^+\mu^-$ decay, the NP contributions are controlled, respectively, by the products $y_R^{\text{ct}}y_S^{\mu\mu}/m_S^2$ in scenario S1 and by $y_R^{\text{ct}}y_P^{\mu\mu}/m_S^2$ in scenario P1. The predicted branching ratio and CP observables of the decay are shown as a function of these products in figure 12. We can see that both $\mathcal{B}(B_s \rightarrow \mu^+\mu^-)$ and $\mathcal{A}_{\Delta\Gamma_s}^{\mu\mu}$ are almost identical for the two scenarios. However, the CP-violating $\mu\mu S$ interaction in scenario P1 can induce a nonzero phase in the Wilson coefficient \mathcal{C}_P , making $\mathcal{S}_{\mu\mu}$ deviate from the SM value of zero. Therefore, we can use the CP observable $\mathcal{S}_{\mu\mu}$ to differentiate between these two scenarios.

5.2 CP-violating tcS couplings

For the tcS interactions given by eq. (2.1), CP violation originates from the nonzero phases of the couplings y_L^{ct} and y_R^{ct} , i.e., $\theta_L \neq 0$ and/or $\theta_R \neq 0$, with the definition $y_L^{\text{ct}} = |y_L^{\text{ct}}|e^{i\theta_L}$ and $y_R^{\text{ct}} = |y_R^{\text{ct}}|e^{i\theta_R}$.⁵ As in the last subsection, we can still choose the four coupling parameters y_R^{ct} , $y_S^{\mu\mu}$, $y_P^{\mu\mu}$ and y_S^{bb} , and consider the two scenarios

⁵Alternatively, one can also use y_S^{ct} and y_P^{ct} as a basis to describe the tcS interactions. Numerical analysis in this basis can be found in appendix A.

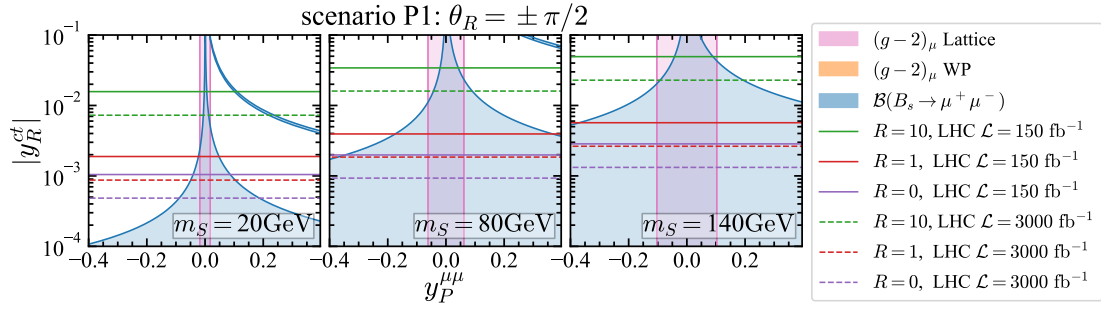


Figure 13: Constraints on the couplings ($|y_R^{ct}|$, $y_P^{\mu\mu}$) in scenario P1 with $y_R^{ct} = \pm i|y_R^{ct}|$. The other captions are the same as in figure 11.

specified by eq. (5.1) to investigate the $B_s \rightarrow \mu^+ \mu^-$ decay, $(g-2)_\mu$ and the LHC direct searches with the decay channel $S \rightarrow \mu^+ \mu^-$, but with a complex y_R^{ct} coupling.

In scenario S1 with a complex y_R^{ct} , all the constraints remain the same as in figure 11, because all the observables considered do not depend on the phase θ_R in this scenario. In scenario P1, on the other hand, the NP contribution to \mathcal{C}_P with a complex y_R^{ct} can interfere with the SM contribution $\mathcal{C}_{10}^{\text{SM}}$, making the constraints from the $B_s \rightarrow \mu^+ \mu^-$ decay different from the ones shown in figure 11. In this case, bounds on $|y_R^{ct}|$ from the branching ratio $\mathcal{B}(B_s \rightarrow \mu^+ \mu^-)$ depend on the phase θ_R , as can be seen from eq. (3.17). In the limit of $\theta_R \rightarrow 0$ or $\pm\pi$, the bounds on $|y_R^{ct}|$ remain the same as in figure 11. In the limit of $\theta_R \rightarrow \pm\pi/2$, i.e., with a maximal magnitude of CP violation, the bounds are shown in figure 13. For other θ_R values, the bounds on $|y_R^{ct}|$ lie between the ones shown in figures 11 and 13. From figure 13, we can see that the constraints from $(g-2)_\mu$ and the direct searches at the LHC remain the same as in scenario P1 with a real y_R^{ct} coupling. For the $B_s \rightarrow \mu^+ \mu^-$ decay, the interference between \mathcal{C}_P and $\mathcal{C}_{10}^{\text{SM}}$ makes the bounds on $|y_R^{ct}|$ much more stringent than the ones in scenario P1 with a real y_R^{ct} coupling. Compared to the other scenarios, in the wider region of the $\mu\mu S$ couplings, the bounds on the tcS coupling are stronger than the expected 95% CL upper bounds at the LHC. In particular, for $m_S = 20$ GeV, the upper bounds on $|y_R^{ct}|$ in most of the $y_P^{\mu\mu}$ regions allowed by $(g-2)_\mu$ are stronger than the expected 95% CL upper bounds at the LHC for $R = 10$.

The complex couplings $y_{L,R}^{ct}$ can also affect the CP observables $\mathcal{A}_{\Delta\Gamma_s}^{\mu\mu}$ and $\mathcal{S}_{\mu\mu}$ of the $B_s \rightarrow \mu^+ \mu^-$ decay, as well as the neutron EDM. In this case, the relevant free parameters include $|y_L^{ct}|$, θ_L , $|y_R^{ct}|$, θ_R , $y_S^{\mu\mu}$, and $y_P^{\mu\mu}$. In order to investigate the constraints from these CP observables, we consider the following four scenarios:

$$(y_R^{ct}, \theta_R, y_L^{ct}, y_S^{\mu\mu}, y_P^{\mu\mu}) = \begin{cases} (|y^{ct}|, \times, |y^{ct}|, v, 0) & \text{scenario S2,} \\ (\times, v, \times, v, 0) & \text{scenario S3,} \\ (|y^{ct}|, \times, |y^{ct}|, 0, v) & \text{scenario P2,} \\ (\times, v, \times, 0, v) & \text{scenario P3,} \end{cases} \quad (5.2)$$

where \times denotes a nonzero entry and v indicates a choice from some benchmark values. Since the $B_s \rightarrow \mu^+ \mu^-$ decay involves only $y_R^{ct} = |y_R^{ct}| e^{i\theta_R}$, while the neutron EDM depends only on $\text{Im}(y_R^{ct} y_L^{ct*}) = |y_R^{ct} y_L^{ct}| \sin(\theta_R - \theta_L)$, a nonzero θ_L shifts only the neutron EDM constraints in the θ_R direction. Therefore, for simplicity, we take $\theta_L = 0$ in the above four scenarios.⁶ It is noted that CP in the lepton sector is conserved in the scenarios S2 and S3, but violated in the scenarios P2 and P3 by the pseudoscalar coupling $y_P^{\mu\mu}$.

In scenarios S2 and P2, where $|y_L^{ct}| = |y_R^{ct}| = |y^{ct}|$, the benchmark values 0.005, 0.05 and 0.1 of $y_S^{\mu\mu}$ (for S2) and $y_P^{\mu\mu}$ (P2) are taken for $m_S = 20, 80$ and 140 GeV, respectively, all of which satisfy the constraints shown in figures 11 and 13. Considering the $B_s \rightarrow \mu^+ \mu^-$ decay and the neutron EDM, constraints on the parameters $(|y^{ct}|, \theta_R)$ are shown in figure 14. The predicted $\mathcal{A}_{\Delta\Gamma_s}^{\mu\mu}$ and $\mathcal{S}_{\mu\mu}$ are also given in figure 14. From this figure, we make the following observations:

- After combining the constraints from $\mathcal{B}(B_s \rightarrow \mu^+ \mu^-)$ and the neutron EDM, the parameter regions with large $|y^{ct}|$ are already excluded. In particular, the neutron EDM excludes the possibility of large NP effect on the $B_s \rightarrow \mu^+ \mu^-$ decay in scenario P2.
- Except in the region of $\theta_R \approx \theta_L$ or $\theta_R \approx \theta_L \pm \pi$, the neutron EDM constraints are compatible with the ones from $\mathcal{B}(B_s \rightarrow \mu^+ \mu^-)$. However, the latter constraints depend on the $\mu\mu S$ couplings. For example, when the $y_S^{\mu\mu}$ and $y_P^{\mu\mu}$ values are smaller than those used in this figure, the constraints from $\mathcal{B}(B_s \rightarrow \mu^+ \mu^-)$ become looser and can even be weaker than from the neutron EDM.
- In scenario S2, the upper bounds from $\mathcal{B}(B_s \rightarrow \mu^+ \mu^-)$ still show a weak dependence on the phase θ_R , which mainly results from the effect of $\mathcal{A}_{\Delta\Gamma_s}^{\mu\mu}$.
- After considering the constraint from $\mathcal{B}(B_s \rightarrow \mu^+ \mu^-)$ and the neutron EDM, the two CP observables $\mathcal{A}_{\Delta\Gamma_s}^{\mu\mu}$ and $\mathcal{S}_{\mu\mu}$ cannot deviate from their corresponding SM predictions by around ± 0.2 in scenario S2 and ± 0.6 in scenario P2, respectively.
- Results for $\theta_L = \pi/4$ are also given in this figure. As expected, the neutron EDM constraints are globally shifted by $\pi/4$ in the θ_R direction, while all the observables of the $B_s \rightarrow \mu^+ \mu^-$ decay remain unchanged.

In scenarios S3 and P3, where $|y_L^{ct}| \neq |y_R^{ct}|$, we consider the benchmark phases $\theta_R = \pm\pi/4, \pm\pi/2, \pm 3\pi/4$.⁷ Constraints on the parameter space in these two scenarios are shown in figures 15 and 16, respectively. In the region with small $|y_L^{ct}|$

⁶In order to illustrate the effect of a nonzero θ_L , we show in figure 14 the results with $\theta_L = \pi/4$.

⁷The cases of $\theta_R = 0$ and $\pm\pi$ respect the CP symmetry in the quark sector and have already been discussed in subsection 5.1.

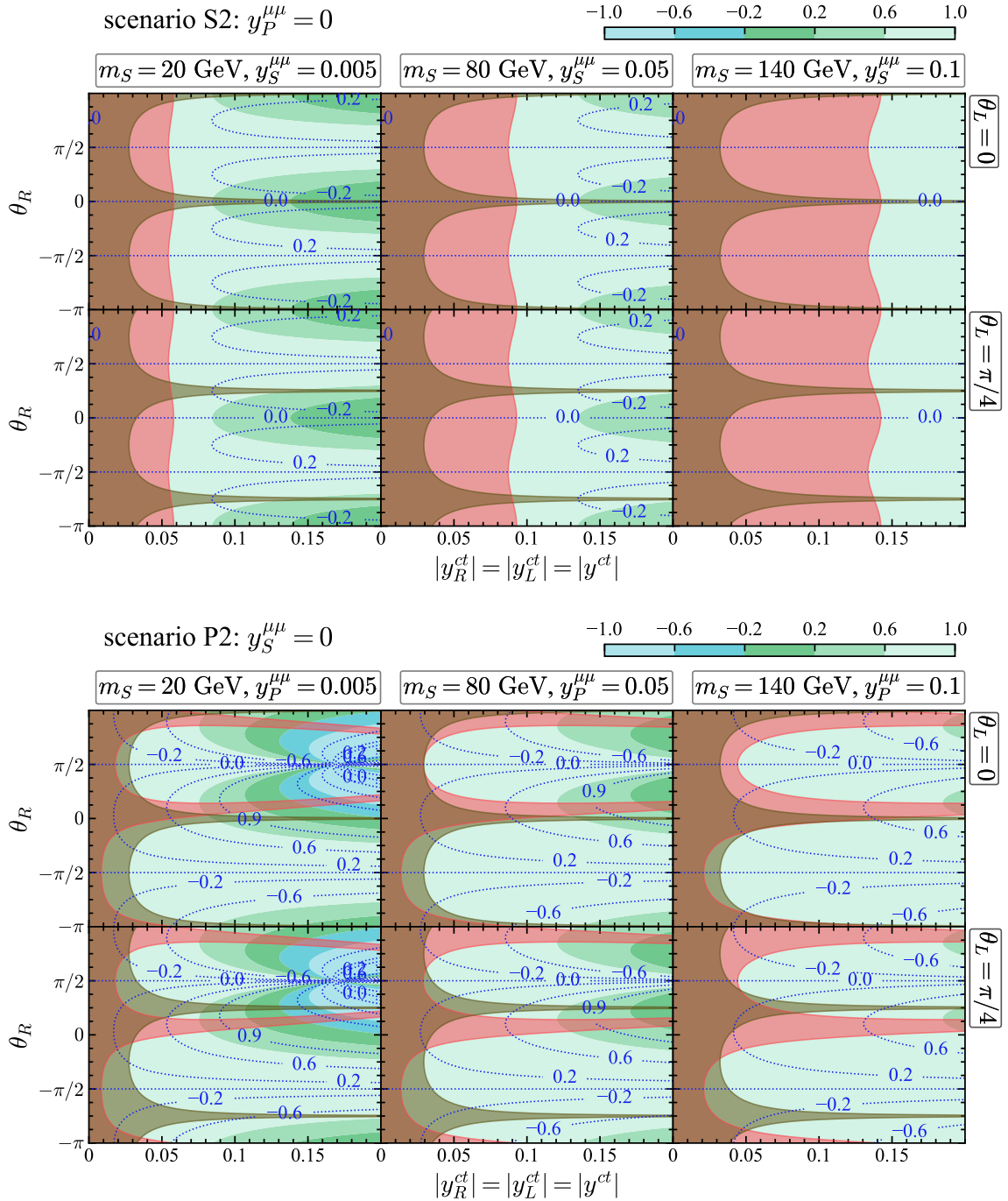


Figure 14: Constraints on $(|y^{ct}|, \theta_R)$ in scenarios S2 (top) and P2 (bottom). The 2σ allowed regions from $\mathcal{B}(B_s \rightarrow \mu^+\mu^-)$ and the 90% CL allowed regions from the neutron EDM are shown in red and gray, respectively. The predicted $\mathcal{A}_{\Delta\Gamma_s}^{\mu\mu}$ and $\mathcal{S}_{\mu\mu}$ are given by the colourmap and the blue curves, respectively. In the second row of each panel, results for $\theta_L = \pi/4$ are shown to illustrate the effect of a nonzero θ_L .

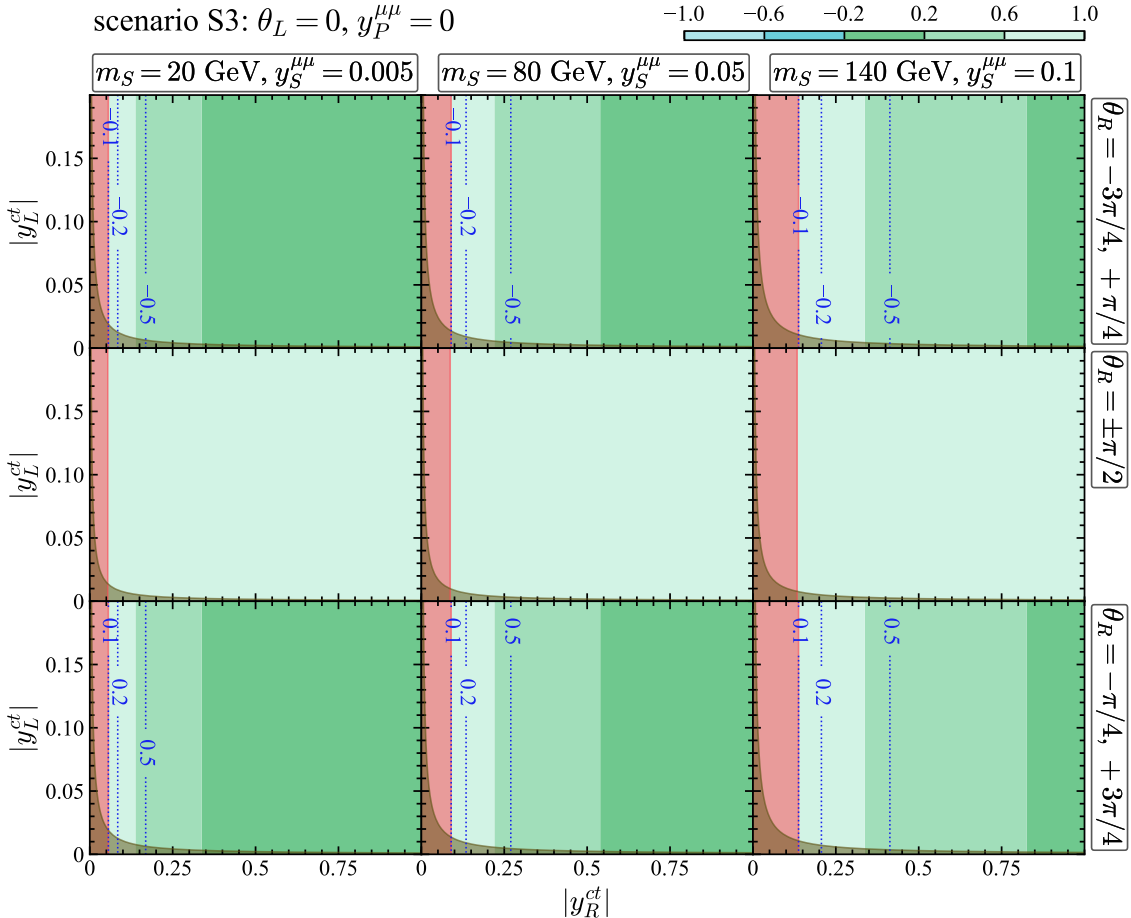


Figure 15: Constraints on $(|y_R^{ct}|, |y_L^{ct}|)$ in scenario S3 for $\theta_R = \pm\pi/4, \pm\pi/2$ and $\pm 3\pi/4$. Here $y_S^{\mu\mu} = 0.005$ (left), 0.05 (middle) and 0.1 (right) are taken for $m_S = 20, 80$ and 140 GeV, respectively. The other captions are the same as in figure 14.

(e.g., smaller than 0.02), the branching ratio $\mathcal{B}(B_s \rightarrow \mu^+\mu^-)$ provides stronger upper bounds on $|y_R^{ct}|$, while the neutron EDM bounds dominate in the region with large $|y_L^{ct}|$ (e.g., larger than 0.05). Within the theoretical framework given in subsection 3.1, it can be proven that both $\mathcal{B}(B_s \rightarrow \mu^+\mu^-)$ and $\mathcal{A}_{\Delta\Gamma_s}^{\mu\mu}$ remain unchanged under $\theta_R \rightarrow \theta_R \pm \pi$ in scenario S3 and $\theta_R \rightarrow -\theta_R \pm \pi$ in scenario P3, which can also be seen from figures 15 and 16, respectively. In scenario P3, this twofold ambiguity can be resolved by the observable $\mathcal{S}_{\mu\mu}$, since its sign is flipped under $\theta_R \rightarrow -\theta_R \pm \pi$. However, in scenario S3, we end up with the degeneracy even after considering $\mathcal{S}_{\mu\mu}$.

From the above numerical analysis, we can see that the $B_s \rightarrow \mu^+\mu^-$ decay and the neutron EDM are complementary to each other in probing the CP phases of the tcS couplings. The advantage of the neutron EDM is that it does not depend on the lepton couplings. In figures 14–16, if the coupling $y_S^{\mu\mu}$ or $y_P^{\mu\mu}$ is taken to be smaller than the benchmark values, the constraints from $\mathcal{B}(B_s \rightarrow \mu^+\mu^-)$ will become looser and could be weaker than the neutron EDM bounds in most of the parameter

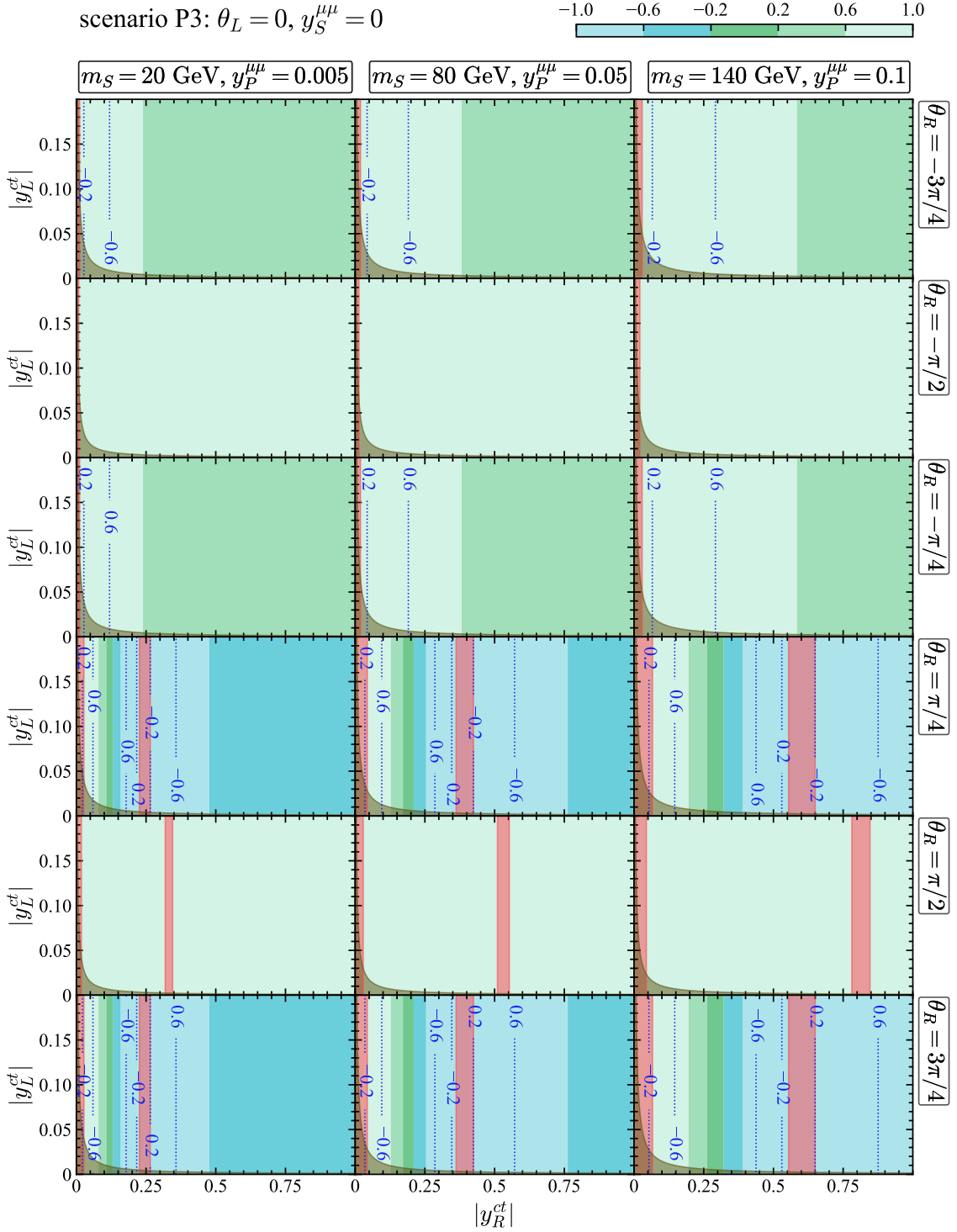


Figure 16: Constraints on $(|y_R^{ct}|, |y_L^{ct}|)$ in scenario P3 for $\theta_R = \pm\pi/4, \pm\pi/2$ and $\pm 3\pi/4$. Here $y_P^{\mu\mu} = 0.005$ (left), 0.05 (middle) and 0.1 (right) are taken for $m_S = 20, 80$ and 140 GeV, respectively. The other captions are the same as in figure 14.

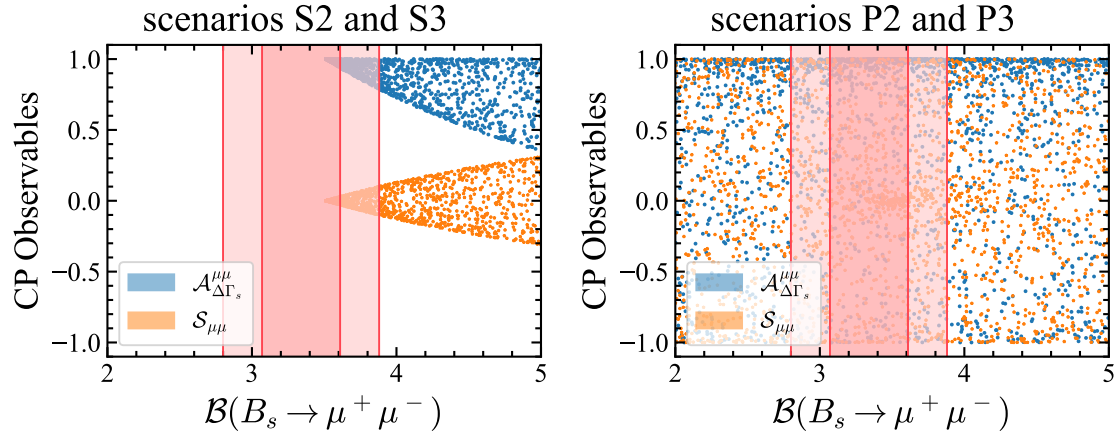


Figure 17: Correlations between the branching ratio and the CP observables of the $B_s \rightarrow \mu^+ \mu^-$ decay in the cases of $y_S^{\mu\mu} \neq 0$ and $y_P^{\mu\mu} = 0$ (left), and $y_S^{\mu\mu} = 0$ and $y_P^{\mu\mu} \neq 0$ (right), with $\theta_L = \theta_R$. The experimental measurement of $\mathcal{B}(B_s \rightarrow \mu^+ \mu^-)$ at the 1σ (dark red band) and 2σ CLs (light red band) are also shown.

spaces. The second advantage is that, when the scalar S becomes heavier, the allowed regions by the neutron EDM remain almost unchanged, while the allowed regions by $\mathcal{B}(B_s \rightarrow \mu^+ \mu^-)$ become much larger. This can be understood as follows: the NP contributions to the $B_s \rightarrow \mu^+ \mu^-$ decay amplitude and the neutron EDM are both proportional to m_S^{-2} ; however, the loop functions $f_{1,2}(x_{tS})$ (cf. eqs. (3.23) and (3.25)) compensate for the m_S^{-2} suppression and make the neutron EDM depend weakly on the scalar mass m_S , which can also be seen from figure 5. For the $B_s \rightarrow \mu^+ \mu^-$ decay, a key benefit is that the CP observables $\mathcal{A}_{\Delta\Gamma_s}^{\mu\mu}$ and $\mathcal{S}_{\mu\mu}$ depend only on the complex phase θ_R . Therefore, maximum deviations of $\mathcal{A}_{\Delta\Gamma_s}^{\mu\mu}$ and $\mathcal{S}_{\mu\mu}$ from their corresponding SM predictions can be achieved in the limit of $\theta_L = \theta_R$, in which the neutron EDM is, however, not affected by the tcS couplings (cf. eqs. (3.22) and (3.24) together with the relation $\text{Re}(y_S^{ct} y_P^{ct*}) = \text{Im}(y_R^{ct} y_L^{ct*})/2$). In this limit, we show in figure 17 the correlations between the branching ratio and the CP observables of the $B_s \rightarrow \mu^+ \mu^-$ decay for $y_S^{\mu\mu} \neq 0$ or $y_P^{\mu\mu} \neq 0$. In this figure, all the parameter points satisfy the constraints from $(g-2)_\mu$ and lie below the expected 95% CL upper bounds at the LHC for $R < 10$. In the case of $y_S^{\mu\mu} \neq 0$ and $y_P^{\mu\mu} = 0$ (including both scenarios S2 and S3), the two CP observables are close to their SM values, namely in the ranges of $0.8 < \mathcal{A}_{\Delta\Gamma_s}^{\mu\mu} < 1.0$ and $-0.1 < \mathcal{S}_{\mu\mu} < 0.1$ after considering the constraints from $\mathcal{B}(B_s \rightarrow \mu^+ \mu^-)$. However, in the case of $y_S^{\mu\mu} = 0$ and $y_P^{\mu\mu} \neq 0$ (including both scenarios P2 and P3), both $\mathcal{A}_{\Delta\Gamma_s}^{\mu\mu}$ and $\mathcal{S}_{\mu\mu}$ can largely deviate from their corresponding SM expectations. In particular, we find that large deviations always correspond to large NP amplitudes, which have even larger magnitudes but different complex phases compared to the SM contribution. Interestingly, such large NP contributions in the limit of $\theta_L = \theta_R$ survive the constraints from all the observables including the neutron

EDM, which can provide constraints only in the general case of $\theta_L \neq \theta_R$.

6 Conclusions

It is known that new scalar singlets under the SM gauge group appear naturally in many well-motivated NP scenarios. In this paper, starting from an EFT framework, we have systematically investigated the effects of a new light scalar singlet S with top-quark FCNC interactions. Its effects on the $B_s \rightarrow \mu^+ \mu^-$ decay, $(g-2)_\mu$ and the neutron EDM are studied in detail. The scalar singlet S can also induce the rare top-quark decay $t \rightarrow cS$ and the single-top production associated with an S at the LHC. Considering the decays of the scalar singlet to a pair of b quarks and/or muons, we have also performed a detailed collider simulation to explore the sensitivity at the current and future LHC to such a scalar singlet S with top-quark FCNC couplings.

It is found that the $B_s \rightarrow \mu^+ \mu^-$ decay involves the same scalar couplings as the LHC direct searches of the scalar S in the three-lepton channel, and can provide an efficient probe of such a scalar singlet. For the $B_s \rightarrow \mu^+ \mu^-$ decay, the scalar singlet S induces two effective operators $\mathcal{O}_{S,P}$ at the b -quark mass scale μ_b . Their Wilson coefficients $\mathcal{C}_{S,P}^{\text{NP}}$ are proportional to the CKM factor $V_{cs}^* V_{tb}$, being much larger than $V_{ts}^* V_{tb}$ associated with the dominant SM contribution $\mathcal{C}_{10}^{\text{SM}}$. Furthermore, the scalar contribution does not suffer from helicity suppression. As a result, the branching ratio of the $B_s \rightarrow \mu^+ \mu^-$ decay provides a strong constraint on the scalar couplings. After considering the constraints from $(g-2)_\mu$, the bounds on $|y_R^{ct}|$ from $\mathcal{B}(B_s \rightarrow \mu^+ \mu^-)$ are stronger than (compatible with) the sensitivity at the LHC with 150 fb^{-1} for $R = y_{S,P}^{bb}/y_{S,P}^{\mu\mu} \approx 10$ in the case that CP is violated (conserving) in the lepton sector.

It should be noted that the tcS couplings $y_{L,R}^{ct}$ (or $y_{S,P}^{ct}$) can generally carry arbitrary CP-violating phases, which are different from the flavour-conserving $\mu\mu S$ and bbS couplings that must be real as required by hermiticity. In this case, the CP observables $\mathcal{A}_{\Delta\Gamma_s}^{\mu\mu}$ and $\mathcal{S}_{\mu\mu}$ of the $B_s \rightarrow \mu^+ \mu^-$ decay provide a useful probe of the CP-violating tcS interactions. We also found that the neutron EDM are very complementary for exploring such CP-violating sources in most of the parameter spaces. However, the neutron EDM depends only on the phase difference $\theta_L - \theta_R$ with $\theta_{L,R}$ denoting the phase of $y_{L,R}^{ct}$, while the $B_s \rightarrow \mu^+ \mu^-$ decay depends only on the phase θ_R . In the special limit of $\theta_L = \theta_R$, the neutron EDM is not affected by the tcS interactions, and only the $B_s \rightarrow \mu^+ \mu^-$ decay can access the CP violation of the tcS couplings. In this limit, maximum deviations of $\mathcal{A}_{\Delta\Gamma_s}^{\mu\mu}$ and $\mathcal{S}_{\mu\mu}$ from their corresponding SM predictions can be achieved. After considering other relevant constraints, the CP observables can lie in the ranges of $\mathcal{A}_{\Delta\Gamma_s}^{\mu\mu} \in (0.8, 1.0)$ and $\mathcal{S}_{\mu\mu} \in (-0.1, 0.1)$ in the case of $y_S^{\mu\mu} \neq 0$ and $y_P^{\mu\mu} = 0$ (including scenarios S2 and S3). On the other hand, the two CP observables can still deviate largely from their SM expectations in the case of $y_S^{\mu\mu} = 0$ and $y_P^{\mu\mu} \neq 0$ (including scenarios P2 and P3), namely $\mathcal{A}_{\Delta\Gamma_s}^{\mu\mu} \in (-1.0, 1.0)$ and $\mathcal{S}_{\mu\mu} \in (-1.0, 1.0)$.

The results obtained in this paper can be applied to the cases with a scalar singlet S being heavier than around 10 GeV. For a scalar singlet S with lower mass, its degree of freedom cannot be integrated out and has to be kept in the low-energy effective Lagrangian when describing the low-energy processes like the $B_s \rightarrow \mu^+ \mu^-$ decay. Furthermore, a light scalar singlet S can even be produced on shell in B -meson decays, and displaced S decays are then needed to be considered. We leave a detailed study of these aspects for future works.

Acknowledgments

This work is supported by the National Natural Science Foundation of China under Grant Nos. 12475094, 12135006, and 12075097, as well as by the self-determined research funds of CCNU from the colleges' basic research and operation of MOE under Grant Nos. CCNU24AI003, CCNU22LJ004 and CCNU19TD012. XY is also supported in part by the Startup Research Funding from CCNU. XY thanks Wei Chao and Jinlin Fu for useful discussions.

A Combined analysis in the scalar and pseudoscalar basis

In this appendix, a combined analysis of the CP-violating tcS couplings is performed in the basis of y_S^{ct} and y_P^{ct} , instead of y_L^{ct} and y_R^{ct} used in subsection 5.2. In this basis, CP violation originates from the nonzero phases of y_S^{ct} and iy_P^{ct} , i.e., $\theta_S \neq 0$ and/or $\theta_P \neq 0$, with the definitions $y_S^{ct} = |y_S^{ct}|e^{i\theta_S}$ and $iy_P^{ct} = |y_P^{ct}|e^{i\theta_P}$. In this case, the relevant free parameters involve $|y_S^{ct}|$, θ_S , $|y_P^{ct}|$, θ_P , $y_S^{\mu\mu}$, and $y_P^{\mu\mu}$. In the numerical analysis, we consider the following four scenarios:

$$(|y_S^{ct}|, \theta_S, |y_P^{ct}|, y_S^{\mu\mu}, y_P^{\mu\mu}) = \begin{cases} (|y^{ct}|, \times, |y^{ct}|, v, 0) & \text{scenario S4,} \\ (\times, v, \times, v, 0) & \text{scenario S5,} \\ (|y^{ct}|, \times, |y^{ct}|, 0, v) & \text{scenario P4,} \\ (\times, v, \times, 0, v) & \text{scenario P5,} \end{cases} \quad (\text{A.1})$$

where $\theta_P = 0$ is assumed, since only the relative phase between y_S^{ct} and iy_P^{ct} enters the CP-violating observables.⁸ In the lepton sector, CP is conserved in scenarios S4 and S5, but violated in scenarios P4 and P5.

In scenarios S4 and P4, we have $|y_S^{ct}| = |y_P^{ct}| = |y^{ct}|$. Constraints on the parameters from the branching ratio $\mathcal{B}(B_s \rightarrow \mu^+ \mu^-)$ and the neutron EDM are shown in figure 18. Furthermore, the predicted CP observables $\mathcal{A}_{\Delta\Gamma_s}^{\mu\mu}$ and $\mathcal{S}_{\mu\mu}$ of the $B_s \rightarrow \mu^+ \mu^-$ decay are also given in figure 18. From this figure, the following observations are made:

⁸In order to illustrate the effects of a nonzero θ_P , results of $\theta_P = \pi/4$ are shown in figure 18.

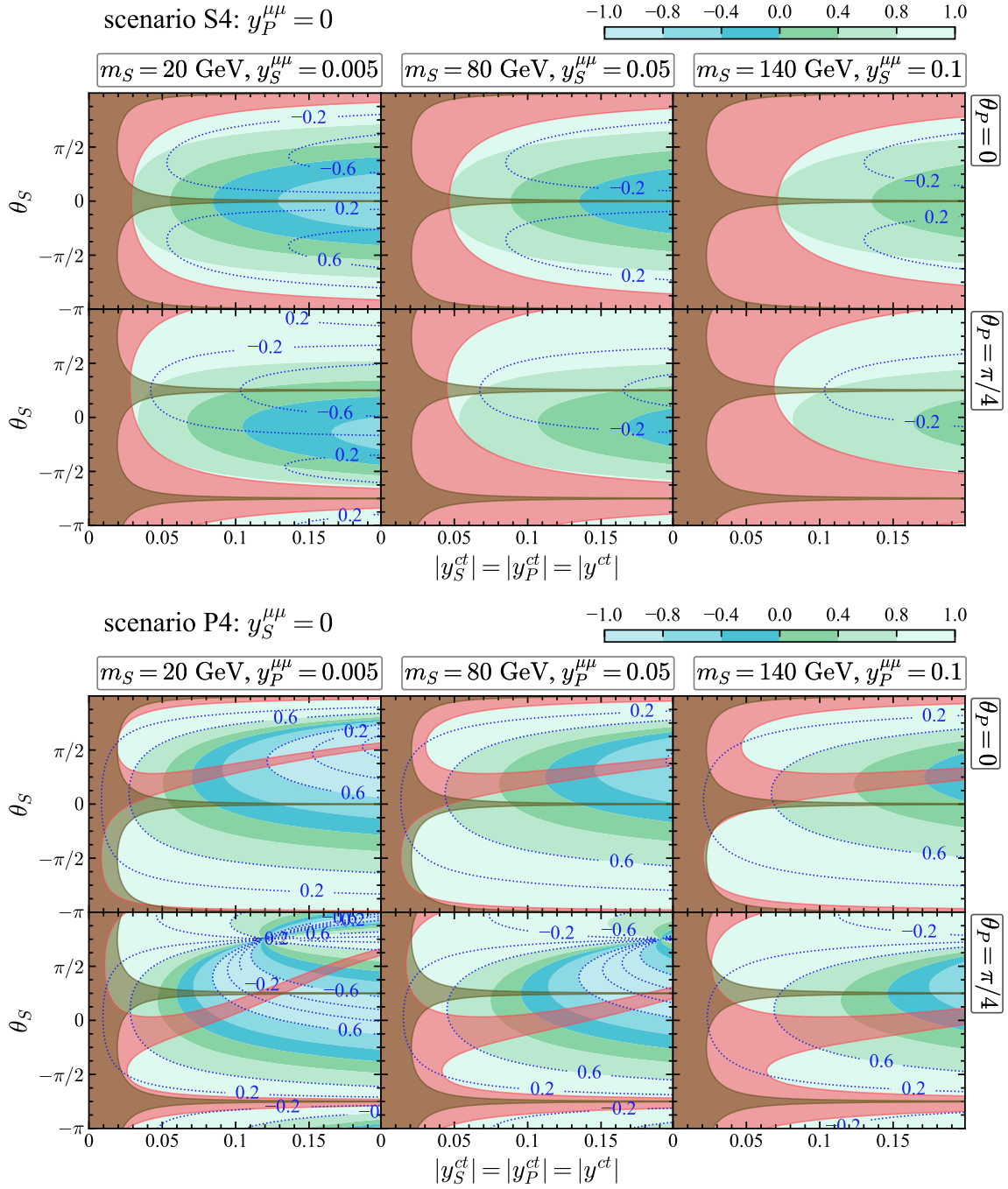


Figure 18: Constraints on $(|y^{ct}|, \theta_S)$ in scenarios S4 (top) and P4 (bottom). In the second row of each panel, results of $\theta_P = \pi/4$ are shown to illustrate the effects of a nonzero θ_P . The other captions are the same as in figure 14.

- In the region far from $\theta_S = \pm\pi$, after combining the constraints from $\mathcal{B}(B_s \rightarrow \mu^+\mu^-)$ and the neutron EDM, the parameter regions with large $|y^{ct}|$ are already excluded. In particular, the regions with large $|y^{ct}|$ allowed by $\mathcal{B}(B_s \rightarrow \mu^+\mu^-)$

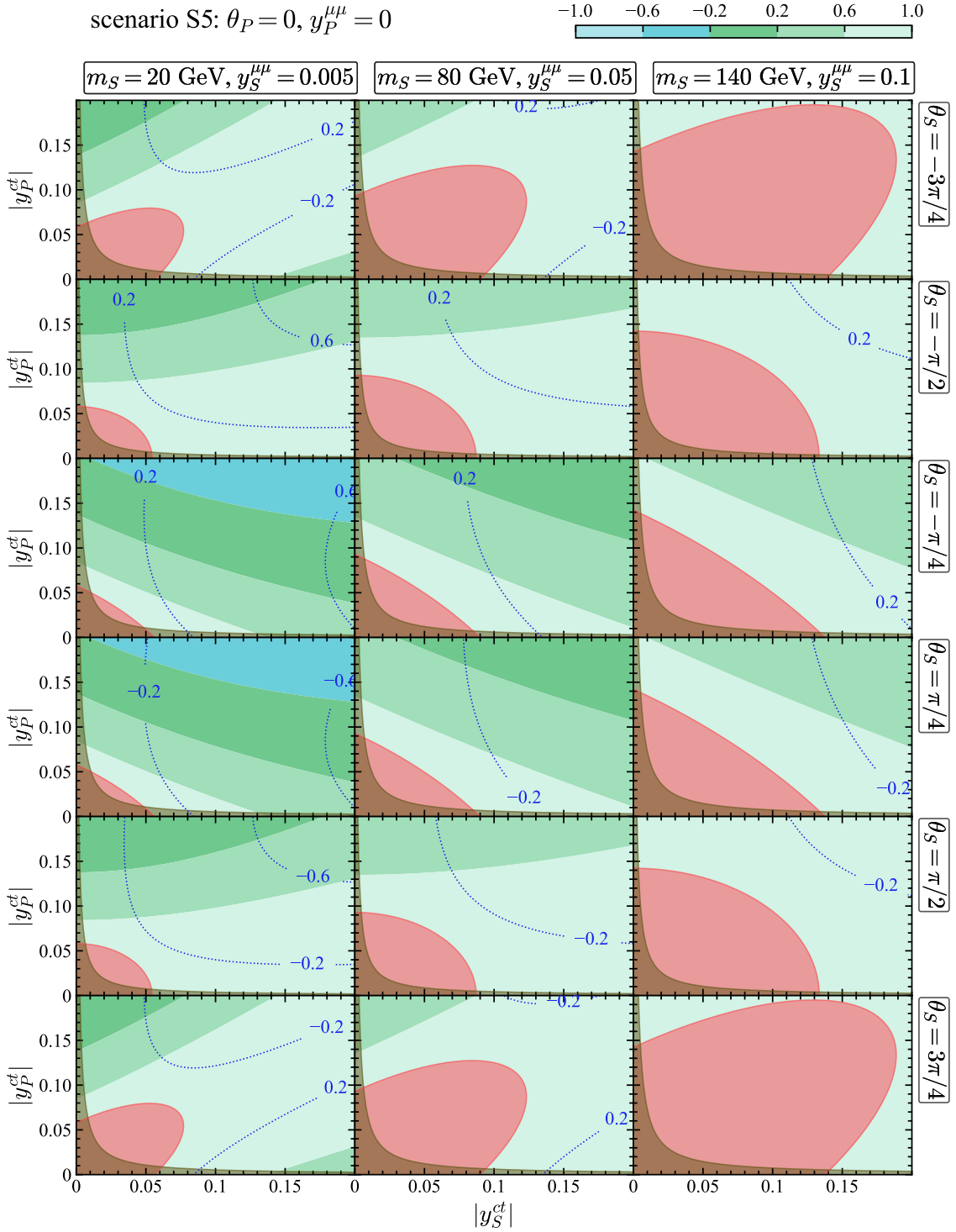


Figure 19: Constraints on $(|y_S^{ct}|, |y_P^{ct}|)$ in scenario S5 for $\theta_S = \pm\pi/4, \pm\pi/2, \pm 3\pi/4$. Here $y_S^{\mu\mu} = 0.005$ (left), 0.05 (middle) and 0.1 (right) are taken for $m_S = 20, 80$ and 140 GeV, respectively. The other captions are the same as in figure 14.

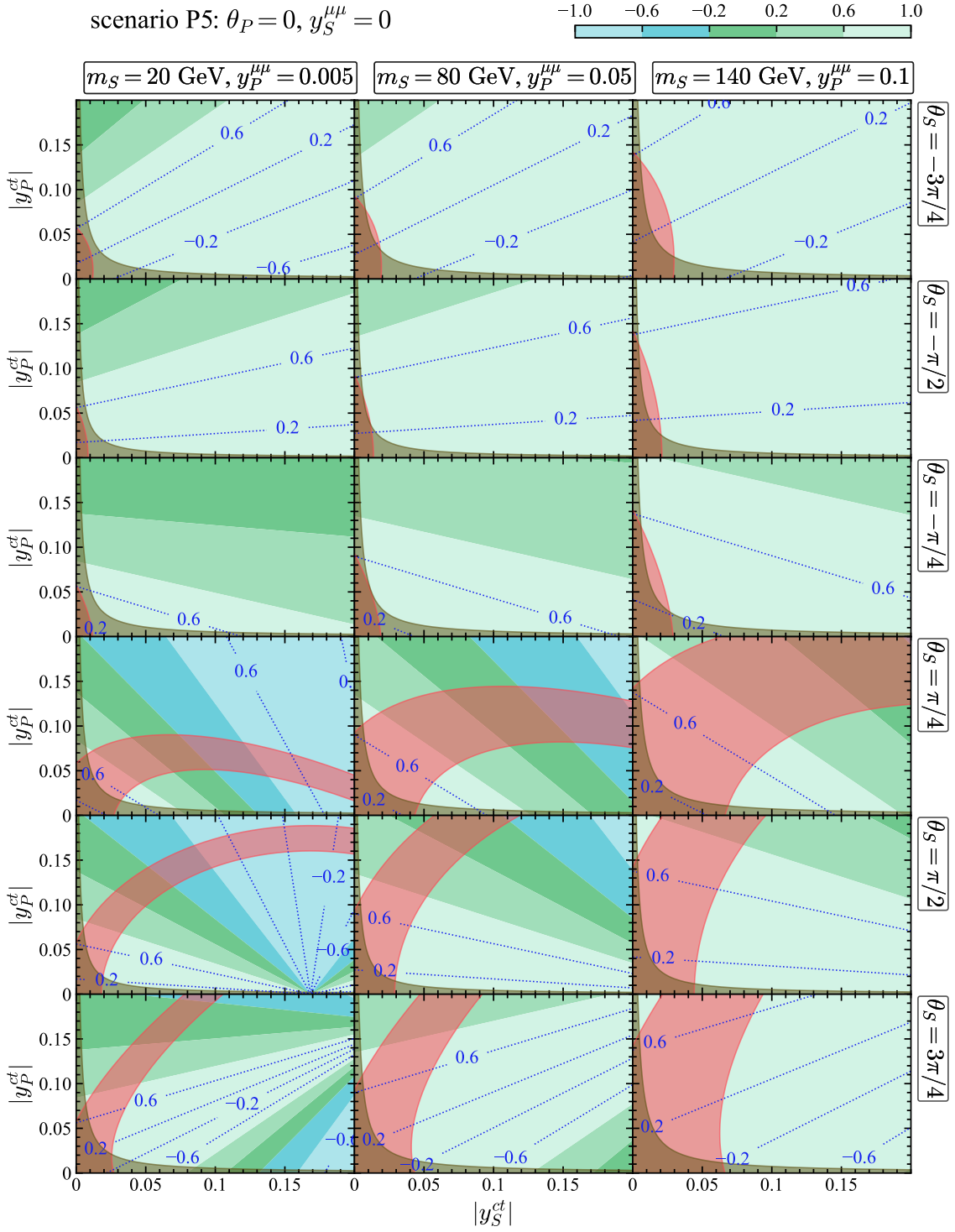


Figure 20: Constraints on $(|y_S^{ct}|, |y_P^{ct}|)$ in scenario P5 for $\theta_S = \pm\pi/4, \pm\pi/2, \pm 3\pi/4$. Here $y_P^{\mu\mu} = 0.005$ (left), 0.05 (middle) and 0.1 (right) are taken for $m_S = 20, 80$ and 140 GeV, respectively. The other captions are the same as in figure 14.

are excluded by the neutron EDM in scenario P4.

- In the region near $\theta_S = \pm\pi$, the constraints from the neutron EDM are stronger than from $\mathcal{B}(B_s \rightarrow \mu^+\mu^-)$. However, when the values of $y_S^{\mu\mu}$ and $y_P^{\mu\mu}$ are larger than the ones used in figure 18, the constraints from $\mathcal{B}(B_s \rightarrow \mu^+\mu^-)$ become more stringent and can even be stronger than the neutron EDM bounds.
- The two CP observables $\mathcal{A}_{\Delta\Gamma_s}^{\mu\mu}$ and $\mathcal{S}_{\mu\mu}$ cannot deviate from their corresponding SM predictions by around ± 0.2 , after considering the constraint from $\mathcal{B}(B_s \rightarrow \mu^+\mu^-)$ and the neutron EDM.

In scenarios S5 and P5 (i.e., $|y_S^{ct}| \neq |y_P^{ct}|$), we consider the benchmark phases $\theta_S = \pm\pi/4, \pm\pi/2$ and $\pm 3\pi/4$,⁹ and show the constraints on the parameter space in figures 19 and 20, respectively. It can be seen that, in the regions with $|y_S^{ct}| \gg |y_P^{ct}|$ or $|y_S^{ct}| \ll |y_P^{ct}|$, the branching ratio $\mathcal{B}(B_s \rightarrow \mu^+\mu^-)$ provides always stronger constraints, even when larger values of $y_{S,P}^{\mu\mu}$ than those used in figures 19 and 20 are considered. In the region with $|y_S^{ct}| \sim |y_P^{ct}|$, the neutron EDM puts more stringent bounds. Especially, as shown in figure 20, the possibility of large NP effects on the $B_s \rightarrow \mu^+\mu^-$ amplitude is excluded by the neutron EDM. In figures 19 and 20, predictions on the CP observables $\mathcal{A}_{\Delta\Gamma_s}^{\mu\mu}$ and $\mathcal{S}_{\mu\mu}$ are also shown. We can see that, different from scenario P5, the cases of $\pm\theta_S$ in scenario S5 (cf. figure 19) cannot be distinguished by $\mathcal{B}(B_s \rightarrow \mu^+\mu^-)$, $\mathcal{A}_{\Delta\Gamma_s}^{\mu\mu}$ or the neutron EDM. However, the observable $\mathcal{S}_{\mu\mu}$ allows us to resolve this twofold ambiguity, since its sign will be different for θ_S and $-\theta_S$.

Since the couplings y_S^{ct} and y_P^{ct} are equivalent to y_L^{ct} and y_R^{ct} for describing the tcS interactions, predictions on the CP observables are the same in these two bases, which are already given in figure 17.

References

- [1] I. Zurbano Fernandez et al., *High-Luminosity Large Hadron Collider (HL-LHC): Technical design report*, *CERN Yellow Reports: Monographs* **10/2020** (2020) .
- [2] PARTICLE DATA GROUP collaboration, *Review of particle physics*, *Phys. Rev. D* **110** (2024) 030001.
- [3] The latest updates can be found at the ATLAS and CMS website: https://atlaspo.cern.ch/public/summary_plots/ and <https://cms-results.web.cern.ch/cms-results/public-results/publications/EX0/>.
- [4] ATLAS collaboration, *Search for high-mass dilepton resonances using 139 fb⁻¹ of pp collision data collected at $\sqrt{s} = 13$ TeV with the ATLAS detector*, *Phys. Lett. B* **796** (2019) 68 [1903.06248].

⁹The cases of $\theta_S = 0$ and $\pm\pi$ respect the CP symmetry in the quark sector and have already been discussed in subsection 5.1.

- [5] CMS collaboration, *Search for resonant and nonresonant new phenomena in high-mass dilepton final states at $\sqrt{s} = 13$ TeV*, *JHEP* **07** (2021) 208 [[2103.02708](#)].
- [6] M. Beneke et al., *Top quark physics*, in *Workshop on Standard Model Physics (and more) at the LHC (First Plenary Meeting)*, pp. 419–529, 3, 2000, DOI [[hep-ph/0003033](#)].
- [7] K. Agashe et al., *Report of the Topical Group on Top quark physics and heavy flavor production for Snowmass 2021*, [2209.11267](#).
- [8] R. Franceschini, *Physics Beyond the Standard Model Associated with the Top Quark*, *Ann. Rev. Nucl. Part. Sci.* **73** (2023) 397 [[2301.04407](#)].
- [9] H. Bahl, S. Koren and L.-T. Wang, *Topopportunities at the LHC: rare top decays with light singlets*, *Eur. Phys. J. C* **84** (2024) 1100 [[2307.11154](#)].
- [10] N.F. Castro and K. Skovpen, *Flavour-Changing Neutral Scalar Interactions of the Top Quark*, *Universe* **8** (2022) 609 [[2210.09641](#)].
- [11] U. Ellwanger, C. Hugonie and A.M. Teixeira, *The Next-to-Minimal Supersymmetric Standard Model*, *Phys. Rept.* **496** (2010) 1 [[0910.1785](#)].
- [12] S. Dimopoulos and J. Preskill, *Massless Composites With Massive Constituents*, *Nucl. Phys. B* **199** (1982) 206.
- [13] D.B. Kaplan and H. Georgi, *$SU(2) \times U(1)$ Breaking by Vacuum Misalignment*, *Phys. Lett. B* **136** (1984) 183.
- [14] D.B. Kaplan, H. Georgi and S. Dimopoulos, *Composite Higgs Scalars*, *Phys. Lett. B* **136** (1984) 187.
- [15] G. Cacciapaglia, G. Ferretti, T. Flacke and H. Serôdio, *Light scalars in composite Higgs models*, *Front. in Phys.* **7** (2019) 22 [[1902.06890](#)].
- [16] C.D. Froggatt and H.B. Nielsen, *Hierarchy of Quark Masses, Cabibbo Angles and CP Violation*, *Nucl. Phys. B* **147** (1979) 277.
- [17] D.E. Morrissey and M.J. Ramsey-Musolf, *Electroweak baryogenesis*, *New J. Phys.* **14** (2012) 125003 [[1206.2942](#)].
- [18] M. Trodden, *Electroweak baryogenesis*, *Rev. Mod. Phys.* **71** (1999) 1463 [[hep-ph/9803479](#)].
- [19] ATLAS collaboration, *Search for flavour-changing neutral-current couplings between the top quark and the Higgs boson in multi-lepton final states in 13 TeV pp collisions with the ATLAS detector*, *Eur. Phys. J. C* **84** (2024) 757 [[2404.02123](#)].
- [20] CMS collaboration, *Search for flavor-changing neutral current interactions of the top quark mediated by a Higgs boson in proton-proton collisions at 13 TeV*, [2407.15172](#).
- [21] S. Banerjee, M. Chala and M. Spannowsky, *Top quark FCNCs in extended Higgs sectors*, *Eur. Phys. J. C* **78** (2018) 683 [[1806.02836](#)].

- [22] N. Castro, M. Chala, A. Peixoto and M. Ramos, *Novel flavour-changing neutral currents in the top quark sector*, *JHEP* **10** (2020) 038 [[2005.09594](#)].
- [23] ATLAS collaboration, *Search for a new scalar resonance in flavour-changing neutral-current top-quark decays $t \rightarrow qX$ ($q = u, c$), with $X \rightarrow b\bar{b}$, in proton-proton collisions at $\sqrt{s} = 13$ TeV with the ATLAS detector*, *JHEP* **07** (2023) 199 [[2301.03902](#)].
- [24] A.J. Buras, F. De Fazio and J. Girrbach, *The Anatomy of Z' and Z with Flavour Changing Neutral Currents in the Flavour Precision Era*, *JHEP* **02** (2013) 116 [[1211.1896](#)].
- [25] A.J. Buras, F. De Fazio, J. Girrbach, R. Knegjens and M. Nagai, *The Anatomy of Neutral Scalars with FCNCs in the Flavour Precision Era*, *JHEP* **06** (2013) 111 [[1303.3723](#)].
- [26] R. Fleischer, R. Jaarsma and G. Tetlalmatzi-Xolocotzi, *In Pursuit of New Physics with $B_{s,d}^0 \rightarrow \ell^+ \ell^-$* , *JHEP* **05** (2017) 156 [[1703.10160](#)].
- [27] R. Fleischer, D.G. Espinosa, R. Jaarsma and G. Tetlalmatzi-Xolocotzi, *CP Violation in Leptonic Rare B_s^0 Decays as a Probe of New Physics*, *Eur. Phys. J. C* **78** (2018) 1 [[1709.04735](#)].
- [28] W. Altmannshofer, C. Niehoff and D.M. Straub, *$B_s \rightarrow \mu^+ \mu^-$ as current and future probe of new physics*, *JHEP* **05** (2017) 076 [[1702.05498](#)].
- [29] ATLAS collaboration, *Study of the rare decays of B_s^0 and B^0 mesons into muon pairs using data collected during 2015 and 2016 with the ATLAS detector*, *JHEP* **04** (2019) 098 [[1812.03017](#)].
- [30] CMS collaboration, *Measurement of the $B_s^0 \rightarrow \mu^+ \mu^-$ decay properties and search for the $B^0 \rightarrow \mu^+ \mu^-$ decay in proton-proton collisions at $\sqrt{s} = 13$ TeV*, *Phys. Lett. B* **842** (2023) 137955 [[2212.10311](#)].
- [31] LHCb collaboration, *Measurement of the $B_s^0 \rightarrow \mu^+ \mu^-$ decay properties and search for the $B^0 \rightarrow \mu^+ \mu^-$ and $B_s^0 \rightarrow \mu^+ \mu^- \gamma$ decays*, *Phys. Rev. D* **105** (2022) 012010 [[2108.09283](#)].
- [32] LHCb collaboration, *Analysis of Neutral B-Meson Decays into Two Muons*, *Phys. Rev. Lett.* **128** (2022) 041801 [[2108.09284](#)].
- [33] G. Buchalla and A.J. Buras, *QCD corrections to rare K and B decays for arbitrary top quark mass*, *Nucl. Phys. B* **400** (1993) 225.
- [34] G. Buchalla and A.J. Buras, *The rare decays $K \rightarrow \pi \nu \bar{\nu}$, $B \rightarrow X \nu \bar{\nu}$ and $B \rightarrow l^+ l^-$: An Update*, *Nucl. Phys. B* **548** (1999) 309 [[hep-ph/9901288](#)].
- [35] M. Misiak and J. Urban, *QCD corrections to FCNC decays mediated by Z penguins and W boxes*, *Phys. Lett. B* **451** (1999) 161 [[hep-ph/9901278](#)].
- [36] T. Hermann, M. Misiak and M. Steinhauser, *Three-loop QCD corrections to $B_s \rightarrow \mu^+ \mu^-$* , *JHEP* **12** (2013) 097 [[1311.1347](#)].

- [37] C. Bobeth, M. Gorbahn and E. Stamou, *Electroweak Corrections to $B_{s,d} \rightarrow \ell^+ \ell^-$* , *Phys. Rev. D* **89** (2014) 034023 [[1311.1348](#)].
- [38] C. Bobeth, M. Gorbahn, T. Hermann, M. Misiak, E. Stamou and M. Steinhauser, *$B_{s,d} \rightarrow l^+ l^-$ in the Standard Model with Reduced Theoretical Uncertainty*, *Phys. Rev. Lett.* **112** (2014) 101801 [[1311.0903](#)].
- [39] M. Czaja and M. Misiak, *Current Status of the Standard Model Prediction for the $B_s \rightarrow \mu^+ \mu^-$ Branching Ratio*, *Symmetry* **16** (2024) 917 [[2407.03810](#)].
- [40] M. Beneke, C. Bobeth and R. Szafron, *Enhanced electromagnetic correction to the rare B-meson decay $B_{s,d} \rightarrow \mu^+ \mu^-$* , *Phys. Rev. Lett.* **120** (2018) 011801 [[1708.09152](#)].
- [41] M. Beneke, C. Bobeth and R. Szafron, *Power-enhanced leading-logarithmic QED corrections to $B_q \rightarrow \mu^+ \mu^-$* , *JHEP* **10** (2019) 232 [[1908.07011](#)].
- [42] T. Feldmann, N. Gubernari, T. Huber and N. Seitz, *Contribution of the electromagnetic dipole operator \mathcal{O}_7 to the $\bar{B}_s \rightarrow \mu^+ \mu^-$ decay amplitude*, *Phys. Rev. D* **107** (2023) 013007 [[2211.04209](#)].
- [43] H.E. Logan and U. Nierste, *$B_{s,d} \rightarrow \ell^+ \ell^-$ in a two Higgs doublet model*, *Nucl. Phys. B* **586** (2000) 39 [[hep-ph/0004139](#)].
- [44] A.J. Buras, R. Fleischer, J. Girrbach and R. Knegjens, *Probing New Physics with the $B_s \rightarrow \mu^+ \mu^-$ Time-Dependent Rate*, *JHEP* **07** (2013) 077 [[1303.3820](#)].
- [45] X.-Q. Li, J. Lu and A. Pich, *$B_{s,d}^0 \rightarrow \ell^+ \ell^-$ Decays in the Aligned Two-Higgs-Doublet Model*, *JHEP* **06** (2014) 022 [[1404.5865](#)].
- [46] C.-W. Chiang, X.-G. He, F. Ye and X.-B. Yuan, *Constraints and Implications on Higgs FCNC Couplings from Precision Measurement of $B_s \rightarrow \mu^+ \mu^-$ Decay*, *Phys. Rev. D* **96** (2017) 035032 [[1703.06289](#)].
- [47] P. Arnan, D. Bećirević, F. Mescia and O. Sumensari, *Two Higgs doublet models and $b \rightarrow s$ exclusive decays*, *Eur. Phys. J. C* **77** (2017) 796 [[1703.03426](#)].
- [48] A. Crivellin, D. Müller and C. Wiegand, *$b \rightarrow s \ell^+ \ell^-$ transitions in two-Higgs-doublet models*, *JHEP* **06** (2019) 119 [[1903.10440](#)].
- [49] M.S. Lang and U. Nierste, *$B_s \rightarrow \mu^+ \mu^-$ in a two-Higgs-doublet model with flavour-changing up-type Yukawa couplings*, *JHEP* **04** (2024) 047 [[2212.11086](#)].
- [50] K. De Bruyn, R. Fleischer, R. Knegjens, P. Koppenburg, M. Merk, A. Pellegrino et al., *Probing New Physics via the $B_s^0 \rightarrow \mu^+ \mu^-$ Effective Lifetime*, *Phys. Rev. Lett.* **109** (2012) 041801 [[1204.1737](#)].
- [51] R. Fleischer, E. Malami, A. Rehult and K.K. Vos, *Targeting (pseudo)-scalar CP violation with $B_s \rightarrow \mu^+ \mu^-$* , *JHEP* **09** (2024) 183 [[2405.10366](#)].
- [52] M. Pospelov and A. Ritz, *Electric dipole moments as probes of new physics*, *Annals Phys.* **318** (2005) 119 [[hep-ph/0504231](#)].

- [53] J. Engel, M.J. Ramsey-Musolf and U. van Kolck, *Electric Dipole Moments of Nucleons, Nuclei, and Atoms: The Standard Model and Beyond*, *Prog. Part. Nucl. Phys.* **71** (2013) 21 [[1303.2371](#)].
- [54] T. Chupp, P. Fierlinger, M. Ramsey-Musolf and J. Singh, *Electric dipole moments of atoms, molecules, nuclei, and particles*, *Rev. Mod. Phys.* **91** (2019) 015001 [[1710.02504](#)].
- [55] R. Alarcon et al., *Electric dipole moments and the search for new physics*, in *Snowmass 2021*, 3, 2022 [[2203.08103](#)].
- [56] R. Franceschini, G.F. Giudice, J.F. Kamenik, M. McCullough, F. Riva, A. Strumia et al., *Digamma, what next?*, *JHEP* **07** (2016) 150 [[1604.06446](#)].
- [57] B. Batell, A. Freitas, A. Ismail, D. McKeen and M. Rai, *Renormalizable models of flavor-specific scalars*, *Phys. Rev. D* **104** (2021) 115032 [[2107.08059](#)].
- [58] CMS collaboration, *Search for low-mass resonances decaying into bottom quark-antiquark pairs in proton-proton collisions at $\sqrt{s} = 13$ TeV*, *Phys. Rev. D* **99** (2019) 012005 [[1810.11822](#)].
- [59] M. Bauer, T. Schell and T. Plehn, *Hunting the Flavon*, *Phys. Rev. D* **94** (2016) 056003 [[1603.06950](#)].
- [60] B. Batell, A. Freitas, A. Ismail and D. McKeen, *Flavor-specific scalar mediators*, *Phys. Rev. D* **98** (2018) 055026 [[1712.10022](#)].
- [61] L.-B. Chen, H.T. Li, J. Wang and Y. Wang, *Analytic result for the top-quark width at next-to-next-to-leading order in QCD*, *Phys. Rev. D* **108** (2023) 054003 [[2212.06341](#)].
- [62] M. Chala, J. Santiago and M. Spannowsky, *Constraining four-fermion operators using rare top decays*, *JHEP* **04** (2019) 014 [[1809.09624](#)].
- [63] Y. Afik, S. Bar-Shalom, A. Soni and J. Wudka, *New flavor physics in di- and tri-lepton events from single-top production at the LHC and beyond*, *Phys. Rev. D* **103** (2021) 075031 [[2101.05286](#)].
- [64] G. Buchalla, A.J. Buras and M.E. Lautenbacher, *Weak decays beyond leading logarithms*, *Rev. Mod. Phys.* **68** (1996) 1125 [[hep-ph/9512380](#)].
- [65] B. Grzadkowski and P. Krawczyk, *HIGGS PARTICLE EFFECTS IN FLAVOR CHANGING TRANSITIONS*, *Z. Phys. C* **18** (1983) 43.
- [66] P. Krawczyk, *Flavor Changing Yukawa Coupling of the Standard Higgs Boson: Effects of the External Quark Masses*, *Z. Phys. C* **44** (1989) 509.
- [67] ATLAS collaboration, *Measurement of the $B_s^0 \rightarrow \mu\mu$ effective lifetime with the ATLAS detector*, *JHEP* **09** (2023) 199 [[2308.01171](#)].
- [68] FLAVOUR LATTICE AVERAGING GROUP (FLAG) collaboration, *FLAG Review 2021*, *Eur. Phys. J. C* **82** (2022) 869 [[2111.09849](#)].

- [69] CKMFITTER GROUP collaboration, *CP violation and the CKM matrix: Assessing the impact of the asymmetric B factories*, *Eur. Phys. J. C* **41** (2005) 1 [[hep-ph/0406184](#)].
- [70] M. Moulson, *Experimental determination of V_{us} from kaon decays*, *PoS CKM2016* (2017) 033 [[1704.04104](#)].
- [71] HFLAV collaboration, *Averages of b-hadron, c-hadron, and τ -lepton properties as of 2021*, *Phys. Rev. D* **107** (2023) 052008 [[2206.07501](#)].
- [72] C. Bobeth and A.J. Buras, *Searching for New Physics with $\overline{B}(B_{s,d} \rightarrow \mu\bar{\mu})/\Delta M_{s,d}$* , *Acta Phys. Polon. B* **52** (2021) 1189 [[2104.09521](#)].
- [73] K. De Bruyn, R. Fleischer, E. Malami and P. van Vliet, *New physics in $B_q^0 - \overline{B}_q^0$ mixing: present challenges, prospects, and implications for*, *J. Phys. G* **50** (2023) 045003 [[2208.14910](#)].
- [74] F. Jegerlehner and A. Nyffeler, *The Muon g-2*, *Phys. Rept.* **477** (2009) 1 [[0902.3360](#)].
- [75] T. Aoyama et al., *The anomalous magnetic moment of the muon in the Standard Model*, *Phys. Rept.* **887** (2020) 1 [[2006.04822](#)].
- [76] MUON G-2 collaboration, *Measurement of the Positive Muon Anomalous Magnetic Moment to 0.20 ppm*, *Phys. Rev. Lett.* **131** (2023) 161802 [[2308.06230](#)].
- [77] CMD-3 collaboration, *Measurement of the $e^+e^- \rightarrow \pi^+\pi^-$ cross section from threshold to 1.2 GeV with the CMD-3 detector*, *Phys. Rev. D* **109** (2024) 112002 [[2302.08834](#)].
- [78] CMD-3 collaboration, *Measurement of the Pion Form Factor with CMD-3 Detector and its Implication to the Hadronic Contribution to Muon (g-2)*, *Phys. Rev. Lett.* **132** (2024) 231903 [[2309.12910](#)].
- [79] S. Borsanyi et al., *Leading hadronic contribution to the muon magnetic moment from lattice QCD*, *Nature* **593** (2021) 51 [[2002.12347](#)].
- [80] A. Boccaletti et al., *High precision calculation of the hadronic vacuum polarisation contribution to the muon anomaly*, [2407.10913](#).
- [81] G. Colangelo et al., *Prospects for precise predictions of a_μ in the Standard Model*, [2203.15810](#).
- [82] F.S. Queiroz and W. Shepherd, *New Physics Contributions to the Muon Anomalous Magnetic Moment: A Numerical Code*, *Phys. Rev. D* **89** (2014) 095024 [[1403.2309](#)].
- [83] G. Blankenburg, J. Ellis and G. Isidori, *Flavour-Changing Decays of a 125 GeV Higgs-like Particle*, *Phys. Lett. B* **712** (2012) 386 [[1202.5704](#)].
- [84] R. Harnik, J. Kopp and J. Zupan, *Flavor Violating Higgs Decays*, *JHEP* **03** (2013) 026 [[1209.1397](#)].

- [85] M. Gorbahn and U. Haisch, *Searching for $t \rightarrow c(u)h$ with dipole moments*, *JHEP* **06** (2014) 033 [[1404.4873](#)].
- [86] G. Boyd, A.K. Gupta, S.P. Trivedi and M.B. Wise, *Effective Hamiltonian for the Electric Dipole Moment of the Neutron*, *Phys. Lett. B* **241** (1990) 584.
- [87] M. Jung and A. Pich, *Electric Dipole Moments in Two-Higgs-Doublet Models*, *JHEP* **04** (2014) 076 [[1308.6283](#)].
- [88] A. Cordero-Cid, J.M. Hernandez, G. Tavares-Velasco and J.J. Toscano, *Bounding the top and bottom electric dipole moments from neutron experimental data*, *J. Phys. G* **35** (2008) 025004 [[0712.0154](#)].
- [89] A.G. Grozin, I.B. Khriplovich and A.S. Rudenko, *Upper limits on electric dipole moments of tau-lepton, heavy quarks, and W-boson*, *Nucl. Phys. B* **821** (2009) 285 [[0902.3059](#)].
- [90] H. Gisbert and J. Ruiz Vidal, *Improved bounds on heavy quark electric dipole moments*, *Phys. Rev. D* **101** (2020) 115010 [[1905.02513](#)].
- [91] Y. Ema, T. Gao and M. Pospelov, *Improved indirect limits on charm and bottom quark EDMs*, *JHEP* **07** (2022) 106 [[2205.11532](#)].
- [92] S. Weinberg, *Larger Higgs Exchange Terms in the Neutron Electric Dipole Moment*, *Phys. Rev. Lett.* **63** (1989) 2333.
- [93] D.A. Dicus, *Neutron Electric Dipole Moment From Charged Higgs Exchange*, *Phys. Rev. D* **41** (1990) 999.
- [94] G. Degrandi, E. Franco, S. Marchetti and L. Silvestrini, *QCD corrections to the electric dipole moment of the neutron in the MSSM*, *JHEP* **11** (2005) 044 [[hep-ph/0510137](#)].
- [95] F. Sala, *A bound on the charm chromo-EDM and its implications*, *JHEP* **03** (2014) 061 [[1312.2589](#)].
- [96] E. Braaten, C.-S. Li and T.-C. Yuan, *The Evolution of Weinberg's Gluonic CP Violation Operator*, *Phys. Rev. Lett.* **64** (1990) 1709.
- [97] D. Chang, W.-Y. Keung, C.S. Li and T.C. Yuan, *QCD Corrections to CP Violation From Color Electric Dipole Moment of b Quark*, *Phys. Lett. B* **241** (1990) 589.
- [98] C. Abel et al., *Measurement of the Permanent Electric Dipole Moment of the Neutron*, *Phys. Rev. Lett.* **124** (2020) 081803 [[2001.11966](#)].
- [99] J. Alwall, R. Frederix, S. Frixione, V. Hirschi, F. Maltoni, O. Mattelaer et al., *The automated computation of tree-level and next-to-leading order differential cross sections, and their matching to parton shower simulations*, *JHEP* **07** (2014) 079 [[1405.0301](#)].
- [100] C. Degrande, C. Duhr, B. Fuks, D. Grellscheid, O. Mattelaer and T. Reiter, *UFO - The Universal FeynRules Output*, *Comput. Phys. Commun.* **183** (2012) 1201 [[1108.2040](#)].

- [101] A. Alloul, N.D. Christensen, C. Degrande, C. Duhr and B. Fuks, *FeynRules 2.0 - A complete toolbox for tree-level phenomenology*, *Comput. Phys. Commun.* **185** (2014) 2250 [[1310.1921](#)].
- [102] C. Bierlich et al., *A comprehensive guide to the physics and usage of PYTHIA 8.3*, *SciPost Phys. Codeb.* **2022** (2022) 8 [[2203.11601](#)].
- [103] DELPHES 3 collaboration, *DELPHES 3, A modular framework for fast simulation of a generic collider experiment*, *JHEP* **02** (2014) 057 [[1307.6346](#)].
- [104] M. Cacciari, G.P. Salam and G. Soyez, *The anti- k_t jet clustering algorithm*, *JHEP* **04** (2008) 063 [[0802.1189](#)].
- [105] E. Conte, B. Fuks and G. Serret, *MadAnalysis 5, A User-Friendly Framework for Collider Phenomenology*, *Comput. Phys. Commun.* **184** (2013) 222 [[1206.1599](#)].
- [106] R.D. Ball et al., *Parton distributions with LHC data*, *Nucl. Phys. B* **867** (2013) 244 [[1207.1303](#)].
- [107] M. Czakon, P. Fiedler and A. Mitov, *Total Top-Quark Pair-Production Cross Section at Hadron Colliders Through $O(\alpha_s^4)$* , *Phys. Rev. Lett.* **110** (2013) 252004 [[1303.6254](#)].
- [108] M. Czakon and A. Mitov, *Top++: A Program for the Calculation of the Top-Pair Cross-Section at Hadron Colliders*, *Comput. Phys. Commun.* **185** (2014) 2930 [[1112.5675](#)].
- [109] A. Bredenstein, A. Denner, S. Dittmaier and S. Pozzorini, *NLO QCD Corrections to Top Anti-Top Bottom Anti-Bottom Production at the LHC: 2. full hadronic results*, *JHEP* **03** (2010) 021 [[1001.4006](#)].
- [110] J.M. Campbell and R.K. Ellis, *$t\bar{t}W^\pm$ production and decay at NLO*, *JHEP* **07** (2012) 052 [[1204.5678](#)].
- [111] N. Kidonakis, *Single-top production in the Standard Model and beyond*, in *13th Conference on the Intersections of Particle and Nuclear Physics*, 8, 2018 [[1808.02934](#)].
- [112] J. Campbell, R.K. Ellis and R. Röntsch, *Single Top Production in Association with a Z Boson at the LHC*, *Phys. Rev. D* **87** (2013) 114006 [[1302.3856](#)].
- [113] J.M. Campbell, R.K. Ellis and C. Williams, *Vector Boson Pair Production at the LHC*, *JHEP* **07** (2011) 018 [[1105.0020](#)].
- [114] G. Cowan, K. Cranmer, E. Gross and O. Vitells, *Asymptotic formulae for likelihood-based tests of new physics*, *Eur. Phys. J. C* **71** (2011) 1554 [[1007.1727](#)].